nature synthesis

Article

https://doi.org/10.1038/s44160-026-01113-5

Multi-walled carbon nanotube network-toughened diamond composite via atomic interface continuity

Received: 11 October 2025

Accepted: 9 June 2026

Published online: 09 July 2026

Check for updates

Jiawei Zhang[1,2,10], Keliang Qiu[3,10], Tengfei Xu[4,5,10], Xi Shen[1,10], Junkai Li[6], Fengjiao Li[1], Richeng Yu[1], Huiyang Gou[6], Duanwei He[7], Liping Wang[8], Zhongzhou Wang[3], Guodong Li[9], Yusheng Zhao[2], Ke Chen[3,9] ✉, Fang Hong[1] ✉, Ruifeng Zhang[4] ✉ & Xiaohui Yu[1] ✉

Enhancing the fracture toughness of diamond while preserving its hardness is a substantial challenge. Most toughening strategies have primarily focused on modulating the internal microstructural units of diamonds, such as adjusting the stacking sequences, faults, nanotwinning and the incorporation of amorphous phases, collectively referred to as intrinsic toughening. Here we introduce an extrinsic toughening strategy to develop a tough diamond composite with complex and abundant sp^2–sp^3-hybridized bonding interfaces by incorporating highly dispersed multi-walled carbon nanotubes (MWCNTs) into the gaps between diamond grains to create a toughened heterogeneous structure containing a three-dimensional continuous MWCNT network. The resultant composite has a hardness of ~91.6 GPa and an average fracture toughness measured using a single-edge notched beam of 31.9 MPa $m^{1/2}$ (with a maximum of 36.4 MPa $m^{1/2}$), which is approximately five times higher than that of single-crystal diamond and even surpasses that of tungsten alloys. The toughening can be attributed to the formation of mixed sp^2–sp^3-hybridized bonding interactions at the three-dimensional continuous MWCNT network/diamond interfaces, which facilitate efficient energy dissipation. Simultaneously, a three-dimensional diamond framework with robust D–D bonding was built, which prevented the loss of hardness due to MWCNT incorporation.

Diamond, with its unique tetrahedral arrangement of sp^3-bonded carbon atoms, is a quintessential engineering material (for example, for cutting tools) that boasts extremely high hardness (60–120 GPa), excellent thermal conductivity and optical transparency[1,2]. However, its low fracture toughness (3.4–5.0 MPa $m^{1/2}$)[3,4] renders it inherently prone to brittle fracture, thereby limiting its broader industrial applications[5]. Enhancing the fracture toughness of diamond typically comes at the expense of its hardness[6], making the simultaneous improvement of both properties a substantial challenge due to the trade-off. In recent decades, several approaches using intrinsic toughening strategies have been developed to enhance the fracture toughness of diamond without sacrificing hardness. These approaches are based on nanostructure engineering, including nanotwinned-diamond architectures[6], graphite–diamond hybrids[7], diamond–graphene composites[8] and amorphous diamond phases[9]. For instance, nanotwin boundaries in diamonds have been shown to be superior to large-angle grain boundaries in enhancing mechanical responses, particularly fracture toughness[6,10–12]. The formation of high-density nanotwins—crystalline

A full list of affiliations appears at the end of the paper. ✉e-mail: chenke0119@buaa.edu.cn; hongfang@iphy.ac.cn; zrf@buaa.edu.cn; yuxh@iphy.ac.cn

regions related by symmetry—can substantially toughen diamond[6]. Recently, a hierarchically structured architecture in diamond that has coherently interfaced polytypes, interwoven nanotwins and interlocked nanograins has achieved a fracture toughness of up to 26.6 MPa $m^{1/2}$, surpassing what can be achieved through nanotwinning alone[5]. For other hard composites, such as ceramics and glass[13], intrinsic toughening strategies have also been reported to improve fracture toughness, for example, bio-inspired structures (based on nacre or enamel)[14], tempering[15] and phase engineering[16]. However, despite these advances, the challenge of enhancing the fracture toughness of diamond using intrinsic toughening strategies but without compromising its high hardness remains unresolved.

Carbon nanotubes (CNTs)—cylindrical derivatives of graphene (with an sp^2-bonded honeycomb lattice)—have excellent mechanical properties and a high aspect ratio, making them ideal candidates over the past two decades for extrinsic reinforcements for toughening diamonds[17,18]. However, the extrinsic toughening mechanisms of CNTs within diamond matrices remain poorly understood and highly debated, with most experimental results falling significantly short of the theoretical predictions when CNTs—either single- or multi-walled—are introduced into various matrices[19].

A key challenge lies in establishing efficient interfacial interactions between the CNTs and the matrix, as fracture toughness is highly dependent on the strength of the interface and the load transfer across it[20,21]. The unique chemical bonds inherent in CNTs often result in lower sliding resistance, akin to the super-lubricity of graphite, which undermines their toughening potential[18,22]. This challenge is clearly demonstrated in CNT/diamond composites, where the absence of chemical bonding reduces interfacial interactions to mere physical contact, substantially compromising toughening effectiveness[18]. Therefore, optimizing the interfacial bonding interactions is crucial for unlocking the full potential of CNTs in diamond composites, especially for achieving notable improvements in toughness, which requires an atomistic understanding of the interface-dominated mechanical behaviour and deep insights into the underlying electronic mechanisms[23].

Beyond interfacial optimization, ensuring structural continuity throughout the composite is equally critical for preventing the formation of mechanically weak diamond islands, a key limitation of earlier heterostructure designs, such as graphene–diamond composites, as isolated diamond domains lead to compromised hardness despite high toughness[24,25]. Creating a uniform hetero-phase structural arrangement is, therefore, essential for promoting positive mechanical responses at multiscale levels, yet this remains a long-standing and critical challenge[5,26,27].

Addressing these dual challenges of interfacial bonding and structural continuity motivates the development of advanced toughening strategies to overcome the brittleness of diamonds without sacrificing their hardness, thereby facilitating their broader commercialization across various applications.

To endow high-hardness diamonds with unprecedented fracture toughness, one avenue worth exploring involves constructing a toughened heterogeneous architecture containing a three-dimensional (3D) continuous network in a diamond matrix. For this purpose, we propose an extrinsic toughening strategy. This strategy introduces highly dispersed multi-walled carbon nanotubes (MWCNTs) into the gaps between diamond grains to create a 3D continuous MWCNT network within the polycrystal diamond matrix (3D-MWCNT–diamond). It uses high-temperature and high-pressure (HTHP) conditions to form a uniform and compact heterogeneous structure in which the MWCNTs are efficiently bonded with the diamond at the continuous MWCNT/diamond interfaces through several bonding interactions, such as sp^2–sp^3 covalent bonds, van der Waals force and physical contact.

Single-edge notched beam (SENB) tests of 3D-MWCNT–diamond found an impressive toughness as high as 36.4 MPa $m^{1/2}$, six times that of single crystal diamond and even surpassing that of tungsten alloys. In situ fracture testing with transmission electron microscopy (TEM) combined with density functional theory (DFT) simulations identified two modes of crack propagation. In regions of 3D-MWCNT/diamond interfaces with relatively weak sp^2 bonding, the crack propagation path was sinuous and wavy, accompanied by deformation of the MWCNTs (pull-out) and interfacial migration. Within the diamond phase, cracks propagated rapidly along the {111} planes in a straight line.

Design, preparation and characterization

The heterogeneous structure of a 3D continuous MWCNT network plus toughened diamond (referred to as 3D-MWCNT–diamond) can be intelligently designed and constructed, as schematically shown in Fig. 1a–e. First, a certain amount of MWCNT fibres is uniformly dispersed into diamond grains. A homogeneous slurry is then prepared by ultrasonic dispersion (Fig. 1a). Next, the water in the slurry is slowly evaporated by simultaneous heating and stirring to produce a mixed powder. The highly dispersed MWCNT fibres are now in the gaps between diamond grains and on the surfaces of diamond grains, thus avoiding the agglomeration of MWCNTs in the diamond matrix (Fig. 1b and Extended Data Fig. 1). Subsequently, a green body is obtained by pre-pressing the prepared mixed MWCNT and diamond powder into a cylindrical bulk as a precursor (Fig. 1c). Finally, a 3D-MWCNT–diamond composite is constructed by transferring the cylindrical precursor into a two-stage multi-anvil apparatus under HTHP conditions (Fig. 1d).

Owing to the inherent ultrahigh strength of diamond, there often exist uneven stress distributions between compressed diamond grains in HTHP conditions[28,29]. Notably, when the preparation temperature is high enough (≥2,000 °C), the strength of the diamond can become partly reduced and the stress deviation will be weakened to some extent[28]. Therefore, when the preparation conditions are rationally optimized, primarily by using an appropriate sintering temperature and suitable pressure, a structurally perfect 3D-MWCNT–diamond composite can be achieved, as shown in Fig. 1e. This is because a low-pressure cavity supported by diamond grains protects the MWCNTs from being transformed into diamond. A high-stress zone can induce the contact point/surface extrusion between diamond grains, which is beneficial for forming strong covalent bonding interactions between the MWCNTs and the diamond or D–D bonds between diamond grains (because of the partial or full transformation of MWCNTs into diamond). Crucially, the presence of the CNTs within these cavities modifies the local conditions, as they create an environment where the pressure is sufficiently low (≲13 GPa) to prevent the CNTs from undergoing the high-pressure phase transition to diamond yet not so low (≳8 GPa) as to trigger severe graphitization of the surrounding diamond matrix. This constitutes a key design trade-off that stabilizes the sp^2-hybridized phase.

To achieve the structurally perfect 3D-MWCNT–diamond composite, we determined the optimal sintering temperature under a pressure of 15 GPa. By observing the fractured surfaces of these samples sintered at various temperatures (800–2,200 °C), we found that at lower sintering temperatures (800–1,800 °C) the densification of the sintered samples was primarily through the fracture of diamond grains (Supplementary Fig. 1a–d). As the sintering progressed, the contact area between diamond particles increased and stress relaxation occurred, so that the densification of the composite reached a limit. However, a significant number of pores persisted, which helped to protect the MWCNTs from the excessive pressure and compression. When the sintering temperature was over 2,000 °C, the diamond grains started to undergo plastic deformation, which reduced the size and number of pores in the sintered samples and enabled further densification and diamond–diamond bonding (Supplementary Fig. 1e,f). X-ray diffraction spectra revealed that the graphite peak vanished in the composite when the sintering temperature exceeded 1,800 °C (Supplementary Fig. 2). This disappearance is attributed to the decrease in diamond strength at higher temperatures, which accelerated the

https://doi.org/10.1038/s44160-026-01113-5

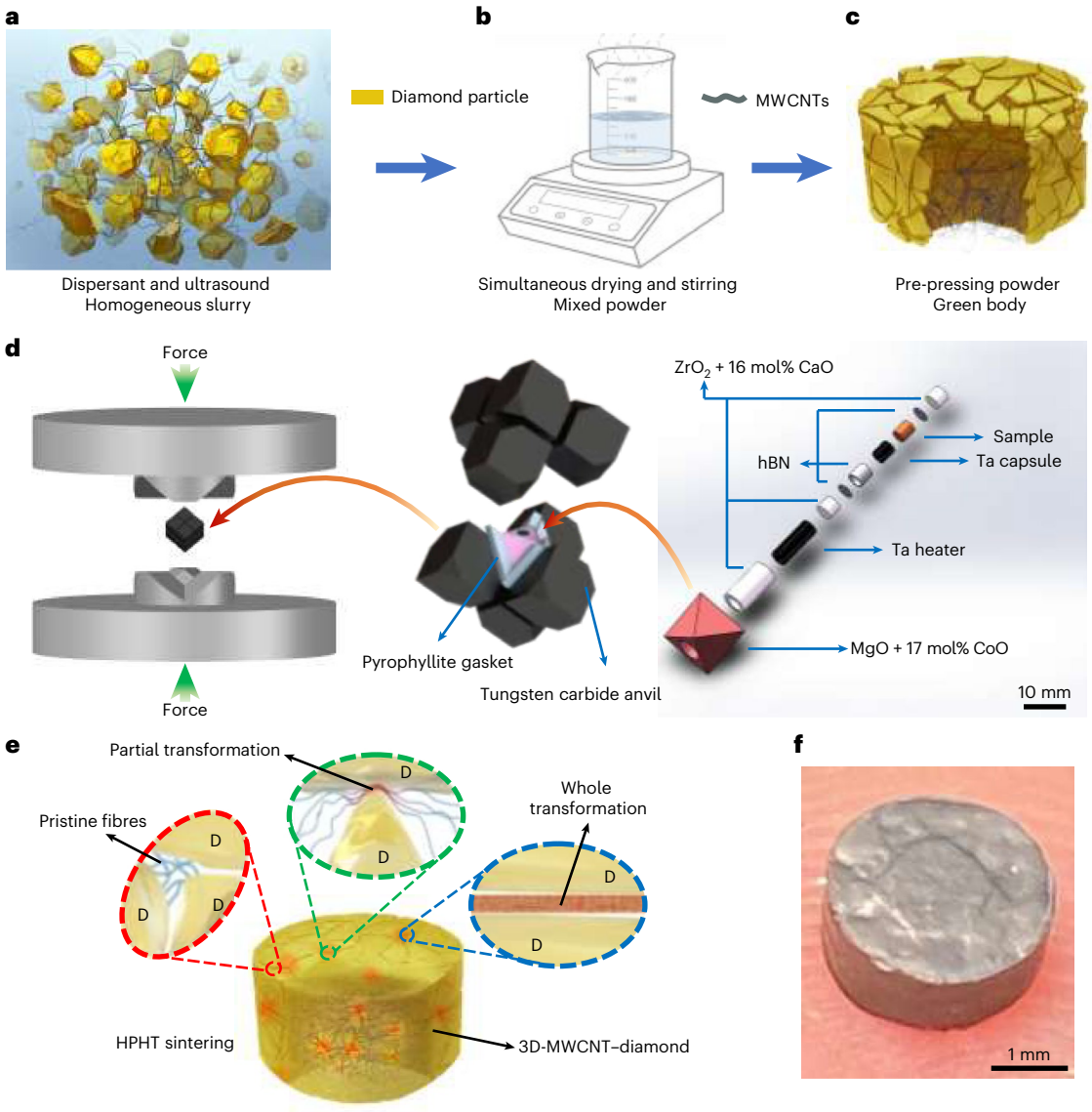

Fig. 1 | Preparation process and structural features of 3D-MWCNT–diamond composite. a–**c**, Schematics of a homogeneous slurry of MWCNTs and diamond (**a**), the preparation of a highly dispersed MWCNT–diamond composite powder (**b**) and the production of a crude green body assembled from the composite powder (**c**). **d**, Multilevel, exploded schematics of a two-stage multi-anvil apparatus based on a Walker-type press, showing the preparation of the composite. **e**, Schematic of a 3D-MWCNT–diamond composite showing structural features. Three enlarged oval insets show three states of MWCNTs within the composite: red, pristine fibres; green, partial transformation into diamond; blue, whole transformation into diamond. Earthy yellow grains represent diamond grains, the black skeleton represents MWCNTs and D indicates diamond. **f**, Optical photograph of the composite bulk (size: 3 mm in diameter and 2 mm in thickness). hBN, hexagonal boron nitride.

plastic deformation of diamond, resulting in an increase in the actual pressure within gaps between diamond grains and the transformation of some compressed MWCNTs into diamond[28]. The absence of graphite peaks in the X-ray diffraction spectrum of the 2,000 °C composite, despite the observation of MWCNTs by scanning transmission electron microscopy (STEM), could have been due to the presence of only a small amount of the graphite phase. A typical cylindrical 3D-MWCNT–diamond composite bulk can be successfully prepared at 2,000 °C and 15 GPa, as shown in Fig. 1f.

We combined scanning electron microscopy (SEM), 3D rendering reconstruction technology and a STEM analysis to systematically characterize the tailored 3D-MWCNT–diamond structure at multiscale levels, as shown in Fig. 2 and Extended Data Figs. 2 and 3. SEM images of typical composite slices show a uniform defect network (dark regions) around diamond particles on a two-dimensional plane (Fig. 2a and Supplementary Fig. 3). The MWCNT fibres as a second phase were fully restricted to these defect regions. A typical assembled image of four continuous slices verified that the heterogeneous structure was uniform (Fig. 2b). We reconstructed 60 continuous slices to form 3D rendering models (10 μm × 6 μm × 1.2 μm) with the software Avizo, which showed that the 3D continuous MWCNT network structure had been perfectly formed (Fig. 2c, top) and was uniformly embedded in the diamond matrix to create an integrated unit (Fig. 2c, bottom). Although the 3D reconstruction was obtained from a specific region, observations at several distinct locations on the sample confirmed the ubiquity of this network structure and supported the representativeness of the reconstruction. The retained 3D continuous MWCNT network had a volume fraction of ~4.6 vol%, which is the average of four independent 3D reconstructions (3.50 vol%, 6.23 vol%, 5.12 vol% and 3.53 vol%). Compared with the initial theoretical volume fraction of ~8.3 vol%, about 45% of the original MWCNT volume had converted to diamond.

https://doi.org/10.1038/s44160-026-01113-5

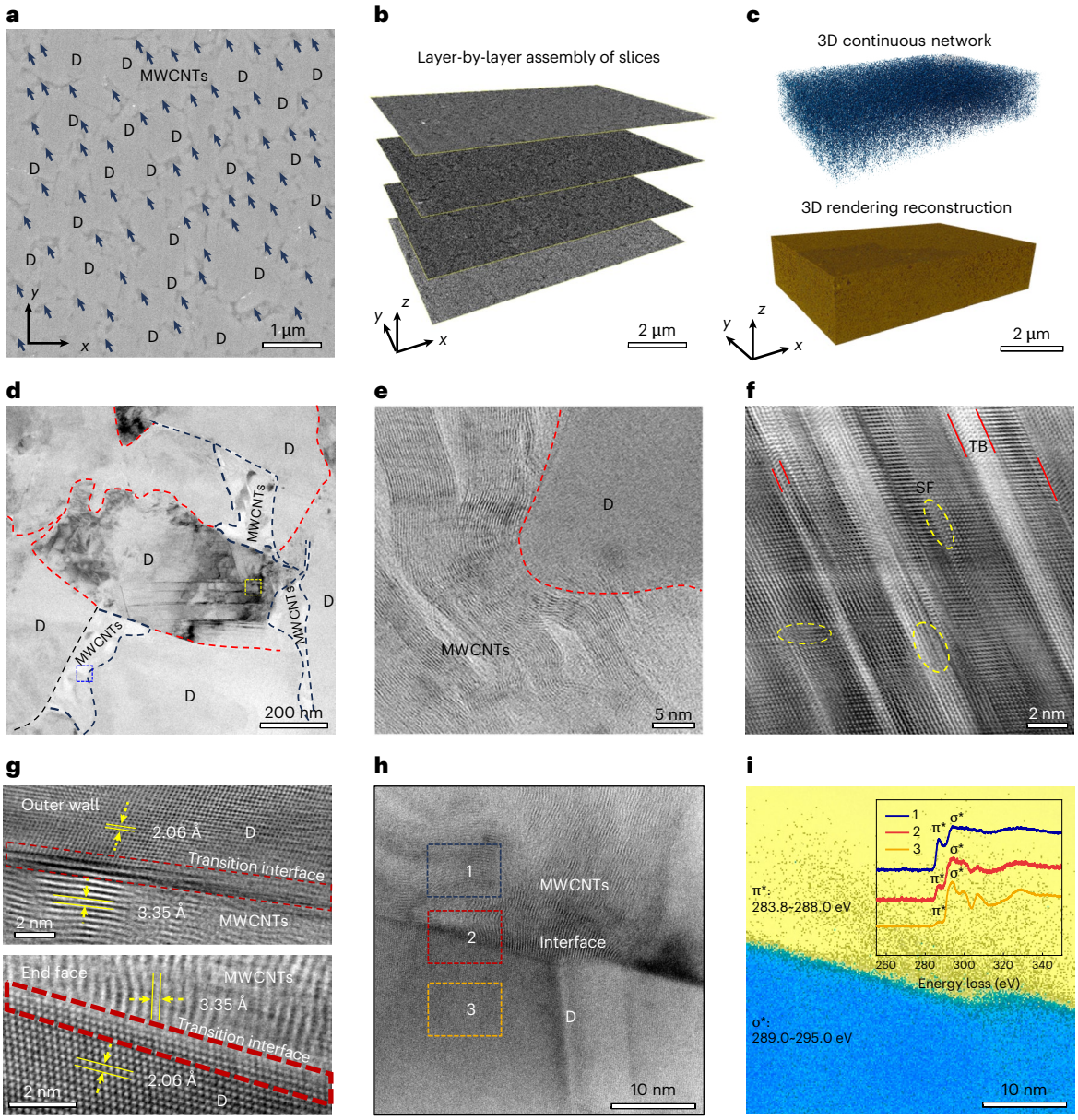

Fig. 2 | Multiscale structural characterization of 3D-MWCNT–diamond composite prepared at 2,000 °C and 15 GPa. a, SEM image of a typical composite slice, obtained by FIB microscopy. Dark blue arrows indicate the gaps around diamond particles. **b**, Layer-by-layer assembly of four slices aligned with the *xy* plane (size 10 μm × 6 μm × 20 nm). Dark spots indicate MWCNTs. **c**, Reconstructed 3D rendering of MWCNTs dispersed in diamond (top) and of the 3D-MWCNT–diamond composite (bottom). The images were produced by analysing typical SEM images of 60 composite slices. **d**, Low-magnification ABF-STEM image of the 3D-MWCNT–diamond composite showing that MWCNTs fill the gaps between diamond grains. **e**, Enlarged ABF-STEM image of a hybrid MWCNT–diamond interface, corresponding to the blue box in **d**, showing that MWCNTs extruded by diamond grains bond well with adjacent diamond grains or phase transform into diamonds. **f**, High-resolution ABF-STEM image of diamond defect structures from MWCNT phase transitions, corresponding to the yellow box in **d**, showing that MWCNTs fully transform into diamond nanotwin bands. Stacking faults are marked in yellow, and twin boundaries are shown in red. **g**, Atomic structure of typical heterogeneous MWCNT/diamond interfaces in the composite characterized by ABF-STEM and viewed along the $[110]_{Diamond}$ direction. The bonding interaction between an MWCNT and diamond occurs at the end face (bottom) or outer wall (top) of an MWCNT. **h**, ABF-STEM image of the MWCNT/diamond interfacial structure. **i**, Corresponding EELS mapping-energy filter image of the same region, showing characteristic π* (yellow) and σ* (blue) peaks. Inset: EELS spectra of different regions in **h** (dark blue box: MWCNTs, red box: the interface, orange box: diamond). The peaks at 285 eV and 292 eV can be attributed to transitions of a C_{1s} electron to the π* and σ* states, corresponding to sp^2 and sp^3 bonding, respectively. The coexistence of blue and yellow at the interface indicates the presence of a transition interface connected by mixed sp^2 and sp^3 bonding. D, diamond; SF, stacking fault; TB, twin boundaries.

Additionally, electrical resistivity measurements (0.01 Ωcm) demonstrated the existence of conductive pathways (Supplementary Fig. 4), which are attributed to the 3D network structure formed by MWCNTs. A low-magnification annular bright-field (ABF) STEM image demonstrated that a tangled, embedded 3D network skeleton of MWCNTs had been perfectly constructed in the gaps between diamond grains (Fig. 2d). Furthermore, we observed direct D–D bonding between adjacent diamond grains, which resulted in a continuous 3D diamond framework that increased the overall hardness of the composite. We also observed that another portion of the same MWCNT fibre situated in a low-pressure cavity had retained its original structure (Extended Data Fig. 3). This continuity of the MWCNT fibre across both regions bridges diamond grains, thus forming the expected 3D continuous MWCNT network structure.

https://doi.org/10.1038/s44160-026-01113-5

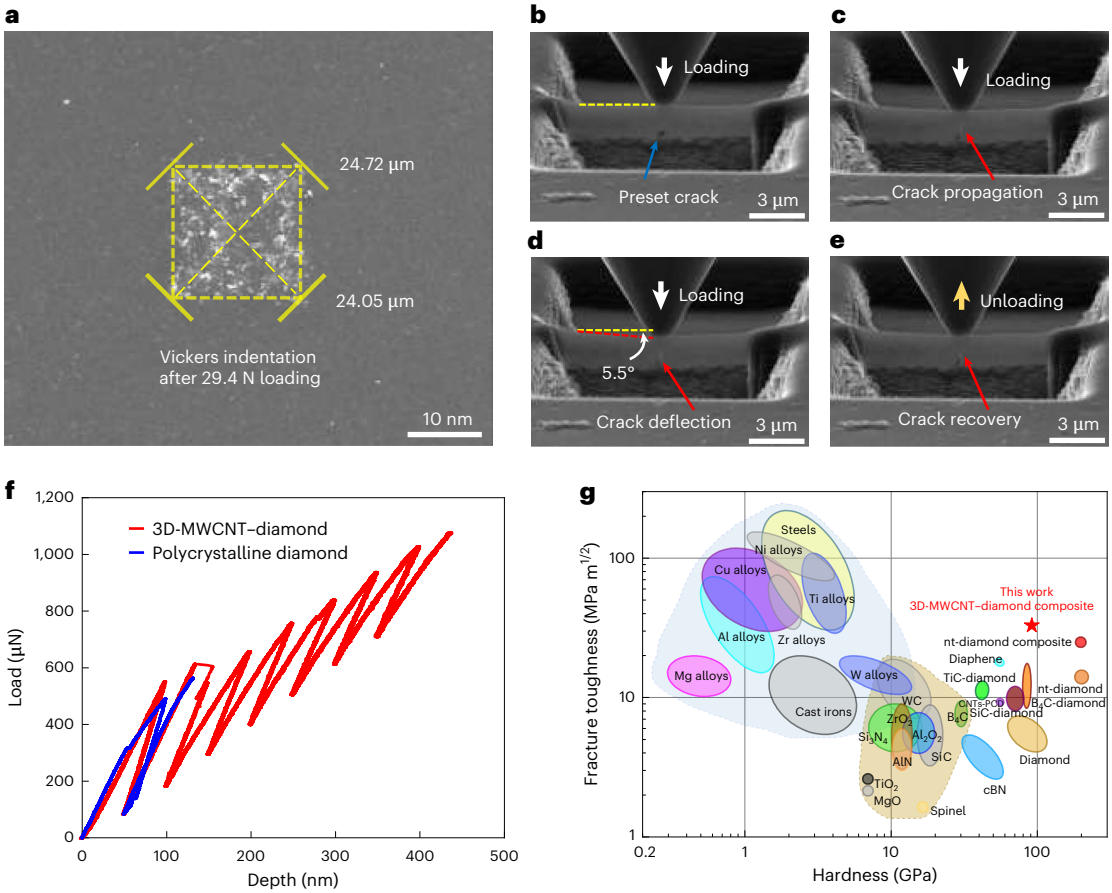

Fig. 3 | Mechanical performance of 3D-MWCNT–diamond composite. **a**, Representative post-indentation SEM image of the composite surface (without conductive coating), after being subjected to a 29.4 N load in a Vickers indentation test. There were no visible indentation cracks. **b**–**e**, Sequential snapshots of the composite micro-beam during the SENB test: at the onset of loading (**b**); at crack propagation from the notch tip (**c**); at the maximum displacement of the diamond indenter is reached, just before the beam fractured completely (**d**) and after unloading (**e**).The white and yellow arrows indicate loading and unloading directions,respectively; the blue arrow marks the pre-cut notch; the red arrows mark propagating cracks; the yellow and red dashed lines denote the initial and deformed upper edges of the micro-beam, respectively. **f**, Typical force–displacement curves of micro-beams made from the 3D-MWCNT–diamond composite and polycrystalline diamond, obtained by the SENB test. **g**, Ashby plot of the hardness against fracture toughness for the composite compared with typical engineering metals, ceramics, superhard materials and other superhard composites. cBN, cubic boron nitride; nt-diamond, nanotwinned diamond; CNT-PDC, composites of carbon nanotubes and polycrystalline diamond.

An enlarged ABF-STEM image confirmed that a portion of the MWCNT fibres in a high-stress zone had bonded well to the adjacent diamond grains (Fig. 2e). A high-resolution ABF-STEM image verified that some partial MWCNTs had transformed into diamond nanotwin bands in high-stress regions after HTHP sintering[30] (Fig. 2f). Consistently, high-resolution TEM observations (Extended Data Fig. 4) revealed intermediate states where the graphitic layers of the MWCNTs had undergone progressive distortion and collapse. The measured interplanar spacings evolved from ~3.36 Å (characteristic of curved graphite layers in CNTs) to ~2.77 Å and then to ~3.03 Å, indicating a structural transition towards diamond. This sequence indicates that the inner layers, under higher curvature and stress, collapsed first and subsequently reconstructed, driving the phase transformation locally. This process aligns well with the wall-collapse and reconstruction mechanism proposed by Pan et al.[30] and is consistent with the localized high-stress conditions in our composite.

In addition, representative ABF-STEM images revealed that the 3D-MWCNT–diamond sample had a highly coherent arrangement at the MWCNT–diamond interface. The coherent bonding interactions between MWCNTs and diamond occurred at either the end face (Fig. 2g, bottom, and Extended Data Fig. 3c) or the outer wall (Fig. 2g, top, and Extended Data Fig. 3d) of the MWCNTs. The bonding was primarily achieved by random sp^3 (the end face) or sp^2 (the outer wall) hybrid covalent bonds formed under HTHP, like the transition interface between graphite and diamond[25]. Moreover, typical electron energy loss spectroscopy (EELS) mapping at the transition interface verified the presence of the coherent interface with mixed sp^2–sp^3 bonding (Fig. 2h,i). This transition interface, connected through mixed sp^2–sp^3 bonding, was formed not only by the direct bonding of MWCNTs to diamond but also by the phase boundary of MWCNT fibres undergoing a partial phase transition, as the middle section under high-stress compression easily transformed into diamond. The EELS profiles revealed an atomic-level sharp interface between MWCNTs and diamond, with a thickness of only a few angstroms (Fig. 2h), confirming direct covalent bonding without an amorphous interlayer. The spatial variability of the interface was primarily topological, as it arose from local geometric factors such as nanotube curvature, contact angle and atomic registry. However, the fundamental nature of the bonding (sp^2–sp^3 hybridization) remained consistent throughout. This covalent interface formed at the physical contact point. As the MWCNT network percolated in three dimensions, these interfaces connected to form a pervasive 3D covalent scaffold, which is crucial for efficient stress transfer.

Mechanical performance

We evaluated the fracture toughness of the free surface of the 3D-MWCNT–diamond composite prepared at 15 GPa and 2,000 °C

https://doi.org/10.1038/s44160-026-01113-5

Table 1 | Fracture toughness of 3D-MWCNT–diamond composite samples (synthesized at 15 GPa and 2,000 °C) from SENB tests

Sample No.	Fracture toughness (MPa m$^{1/2}$)		
	Measured value	Average value	Median value
1	27.3		
2	26.7		
3	36.4	31.9 ± 4.6	33.8
4	35.5		
5	33.8		

using an indentation fracture method[28]. Interestingly, after a large load (29.4 N) had been applied to the free surface of the composite, there were no cracks visible in the post-indentation image (Fig. 3a), indicating its high fracture toughness. Attempts to obtain the indentation toughness at higher loads failed. At 49 N, there were still no cracks (Supplementary Fig. 6a), and at 98 N, the indenters were damaged (Supplementary Fig. 6c).

We performed SENB tests on the composite sample to accurately estimate its fracture toughness (Fig. 3b–f, Supplementary Fig. 5 and Supplementary Video 1). As the top diamond indenter was pressed down, a crack initiated at the tip of the precut notch, which first propagated to the upper left (Fig. 3c) and then turned nearly 45° and extended to the upper right (Fig. 3d). This large-angle crack deflection consumed energy[31], demonstrating the exceptional fracture toughness of the 3D-MWCNT–diamond composite. After retracting the probe (Fig. 3e), the crack healed to a considerable extent. The SENB tests found that the average fracture toughness of the composite micro-beam was 31.9 ± 4.6 MPa m$^{1/2}$ and reached a maximum of 36.4 MPa m$^{1/2}$ (Table 1). We validated the reliability of the SENB method with control experiments on both a WC–6Co benchmark (indentation 11.5 ± 0.7 MPa m$^{1/2}$ and SENB 14.3 ± 1.6 MPa m$^{1/2}$) and pure polycrystalline diamond prepared at 15 GPa and 2,200 °C (indentation 12.4 ± 2.5 MPa m$^{1/2}$ and SENB 16.5 ± 2.3 MPa m$^{1/2}$), each showing the expected ~25% systematic overestimation of SENB over the Vickers indentation toughness (Extended Data Fig. 5c), consistent with the previously reported difference[5]. This systematic overestimation is stable and reproducible. The average SENB toughness of the composite (31.9 MPa m$^{1/2}$; equivalent Vickers indentation toughness ~25.5 MPa m$^{1/2}$) is approximately five times higher than that of single-crystal diamond, 1.8 times higher than that of the pure polycrystalline diamond control synthesized (15 GPa at 2,000 °C) under identical conditions (14.0 MPa m$^{1/2}$; Supplementary Fig. 6d) and 1.2 times higher than that of the toughest hierarchically structured diamond composite (26.6 MPa m$^{1/2}$)[5]. This substantial enhancement is conclusively attributed to the 3D-MWCNT network. Moreover, we confirmed that the Vickers hardness of the composite was 91.6 ± 3.1 GPa under a 29.4 N load, comparable with that of single-crystal diamond[1,6].

We compared the toughness and hardness of some typical engineering metals, ceramics, superhard materials (for example, diamond and nanotwinned diamond) and other superhard composites (for example, B_4C-diamond, TiC-diamond and nanotwinned-diamond composite), which highlighted the unique combination of fracture toughness and high hardness exhibited by the 3D-MWCNT–diamond composite[5,6,18,24,32–41] (Fig. 3g). Moreover, a direct toughness comparison with a typical tungsten alloy (97W–2Ni–1Fe) showed that its SENB toughness (25.6 MPa m$^{1/2}$; Supplementary Fig. 6h) was lower than that of our composite, further confirming that the composite exceeds the toughness of tungsten alloys.

We obtained the optimal combination of fracture toughness and hardness of the composite by controlling the sintering temperature from 1,400 °C to 2,200 °C to form the special 3D continuous MWCNT network structure under 15 GPa, as shown in Extended Data Fig. 5b. As the sintering temperature was gradually increased, the hardness of the composite was enhanced step by step from 50.2 ± 3.4 GPa for 1,400 °C to 91.6 ± 3.1 GPa for 2,000 °C, 97.5 GPa for 2,100 °C and 99.4 ± 3.6 GPa for 2,200 °C. The fracture toughness of the composite increased from 8.0 ± 3.4 MPa m$^{1/2}$ for 1,400 °C to 31.9 ± 4.6 MPa m$^{1/2}$ for 2,000 °C (Extended Data Fig. 5d) and then suddenly decreased to 14.5 ± 2.5 MPa m$^{1/2}$ for 2,100 °C (Extended Data Fig. 5e) and further to 12.4 ± 2.3 MPa m$^{1/2}$ for 2,200 °C (Extended Data Fig. 5f). Obviously, with a lower sintering temperature of 1,400 °C, sintering did not produce good interface bonding, resulting in a low hardness and low fracture toughness. However, when the temperature was increased to 2,200 °C, obvious cracks appeared at the four corners of the Vickers indentation (Extended Data Fig. 5f), indicating its low fracture toughness. The 3D-MWCNT–diamond became less tough when the sintering temperature was more than 2,000 °C because more MWCNTs were transformed into diamond. As shown in Supplementary Fig. 7c,d, the 3D rendering of the 2,100 °C sample confirms the absence of a pervasive fibrous network[28]. Moreover, the sample even gradually became transparent as the temperature was increased (inset in Extended Data Fig. 5f). By contrast, the hardness of 3D-MWCNT–diamond almost linearly increased with temperature because the sample densified and the diamond bonding was strengthened. Thus, we obtained the optimum conditions (15 GPa and 2,000 °C) for preparing 3D-MWCNT–diamond to realize high hardness and high fracture toughness from the above experiments. The aforementioned changes in hardness and toughness under HTHP conditions (Supplementary Information) primarily resulted from the evolution of the microstructure of the composite (Supplementary Fig. 1), the phase composition (Supplementary Fig. 2) and the interfacial bonding strength.

Toughening mechanism

To elucidate the toughening mechanism at the nanoscale, we conducted an in situ tensile fracture test using TEM on a specially designed 3D-MWCNT–diamond composite slice, as shown in Fig. 4a and Extended Data Fig. 6 (Supplementary Fig. 8 and 9). During the test, a stress concentration region initially formed near the narrowest point (Fig. 4a, $\varepsilon = 0\%$), which acted as a crack initiation source. With an increase in the strain to $\varepsilon = 1.58\%$, there was no crack initiation from the narrowest point. When the strain was increased to about 1.75% (Supplementary Video 2), a crack initiated near the narrowest point, which instantaneously propagated until the sample fractured suddenly at a strain of 1.81%. The whole crack propagation path in the region where MWCNTs are incorporated into the composite exhibited frequent changes and deflections. The enlarged TEM images in Fig. 4b,c and Extended Data Fig. 6a, corresponding to the different colour boxes in Fig. 4a ($\varepsilon = 1.81\%$) show that the cracks have sinuous and jagged propagating paths within the composite phase (region 1, Extended Data Fig. 6b), whereas they propagate along the {111} plane in a straight line within the diamond phase (region 2), consistent with the brittle fracture mode of a single diamond (Extended Data Fig. 6c). The tensile experiments consistently demonstrated the special fracture mode of the 3D-MWCNT–diamond composite (Supplementary Figs. 8 and 9).

This deflected behaviour within the composite may be attributed to the non-uniform internal stress distribution between the MWCNTs and the diamond matrix[25,30], because the relatively weak bonding interaction at the MWCNT/diamond interface easily leads to crack deflections, which contributes to the toughening[5]. Usually, the composite can sustain high loads due to the load transfer arising from the mismatch in elastic moduli between the MWCNTs and the diamond matrix.

Furthermore, the high-magnification TEM images demonstrated that the MWCNTs were pulled out (Fig. 4b) and that the diamond grains were bridged by MWCNTs (Fig. 4c) at the fracture regions. Obviously, the presence of MWCNTs (Fig. 2e) and diamond defect structures,

https://doi.org/10.1038/s44160-026-01113-5

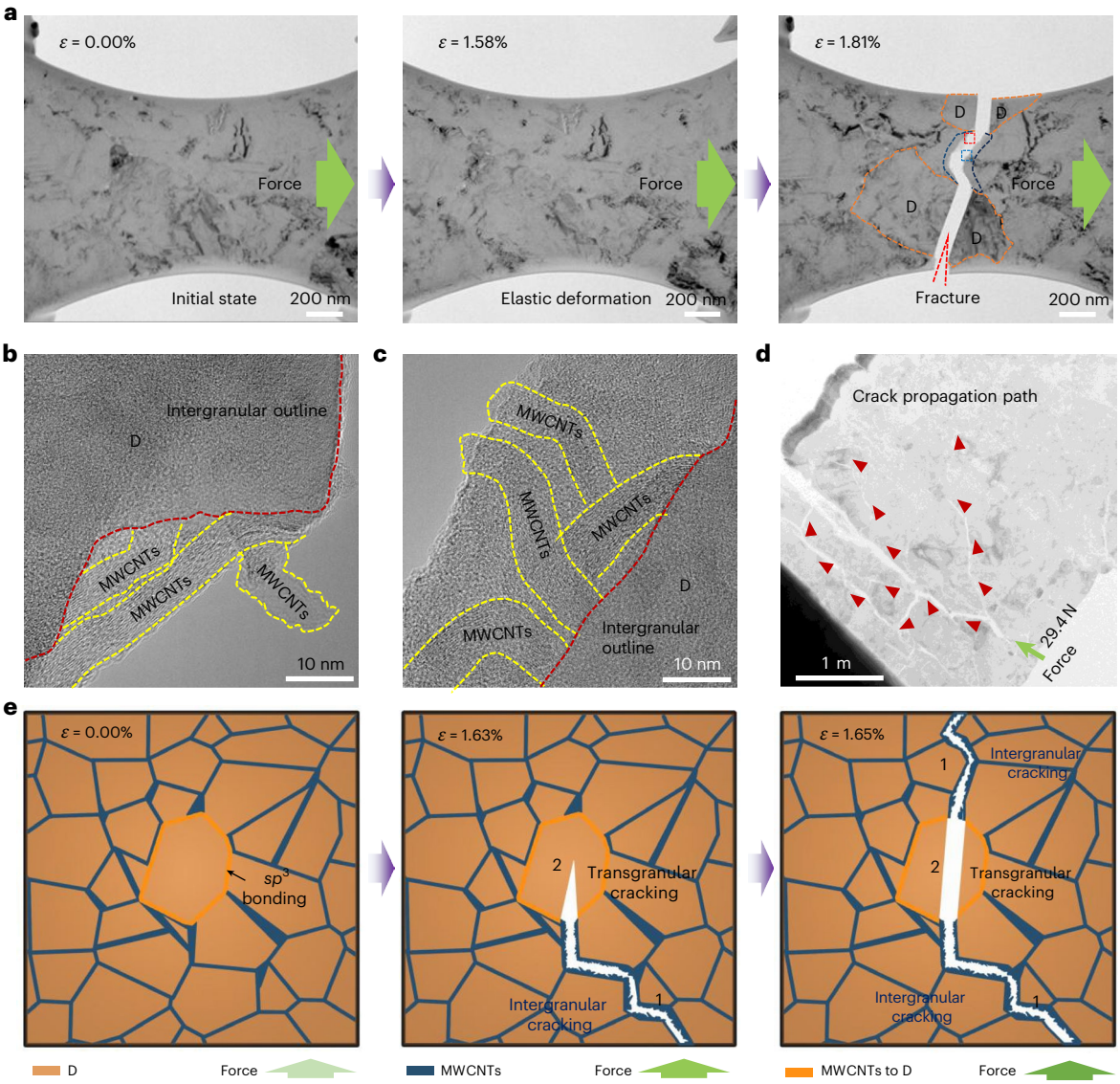

Fig. 4 | Toughening mechanism of 3D-MWCNT–diamond composite revealed by in situ TEM. a, Bright-field images of a composite slice at different tensile strains (ε = 0, 1.58% and 1.81%). The orange dashed lines show a transgranular cracking region of the diamond grain. The dark blue dashed lines indicate the intergranular cracking regions. **b**,**c**, Enlarged TEM images, corresponding to the red and blue boxes in **a**, showing the pull-out (**b**) and bridging (**c**) of MWCNTs. The dark red dashed lines represent the intergranular crack outline of the composite. **d**, Low-magnification ABF-STEM image of composite microcracks under Vickers indentation, revealing a radiating multi-branched fracture path. Red arrows represent microcrack propagation paths. **e**, Sketch maps of this composite at three stages (ε = 0%, 1.63%, and 1.65%) show the microcrack propagation paths of the composite more clearly during the tensile process. The weak bonding interfaces that separate the grains are denoted by the dark blue regions, and the strong covalent interfaces that bond the grains are represented by the orange regions. The intergranular cracking region (1) that separates the grains is denoted by the frayed dark blue line, and the transgranular cracking region (2) of the grain is denoted by the orange line.

like stacking faults and diamond nanotwin bundles[31] (Fig. 2f and Extended Data Fig. 7i), leads to sinuous and wavy boundaries with tapered fracture edges on each fractured surface. Therefore, the fracture edges of the composite exhibited a conical shape, which is a characteristic of the pull-out fracture mode. This fracture mode is conducive to energy dissipation and toughening of the material[5], as it allows for a gradual release of the stress and prevents sudden, catastrophic failure.

Typical STEM images show that the overall crack pattern exhibited a radiating multi-branched fracture path on the composite surface under indentation (Fig. 4d and Extended Data Fig. 7a,b), which effectively dispersed the external load and minimized the stress concentration. Actually, the large energy dissipation associated with large crack deflection effectively reduced the local stress and strain, which made the composite tougher.

Based on the above experimental observations, we propose that when the force was initially applied, a microcrack easily initiated at the relatively weak interface of MWCNT/diamond with sp^2 bonding. When the strain was increased to 1.78%, a crack propagated and deflected along the diamond due to the strong interfacial hindrance. This was simultaneously accompanied by the deformation (pull-out) of MWCNTs, leading to intergranular cracking (region 1). Subsequently, when a propagating crack reached a diamond region, it often traversed the entire diamond grain with a transgranular cracking mode (region 2), which facilitated the dispersion and transfer of the load to the diamond grains, which were interconnected by the strong sp^3 bonding of MWCNTs. When the strain was increased to 1.81%, the crack continued to propagate along the MWCNT/diamond interface until the sample fully fractured with the intergranular cracking mode. Consequently,

https://doi.org/10.1038/s44160-026-01113-5

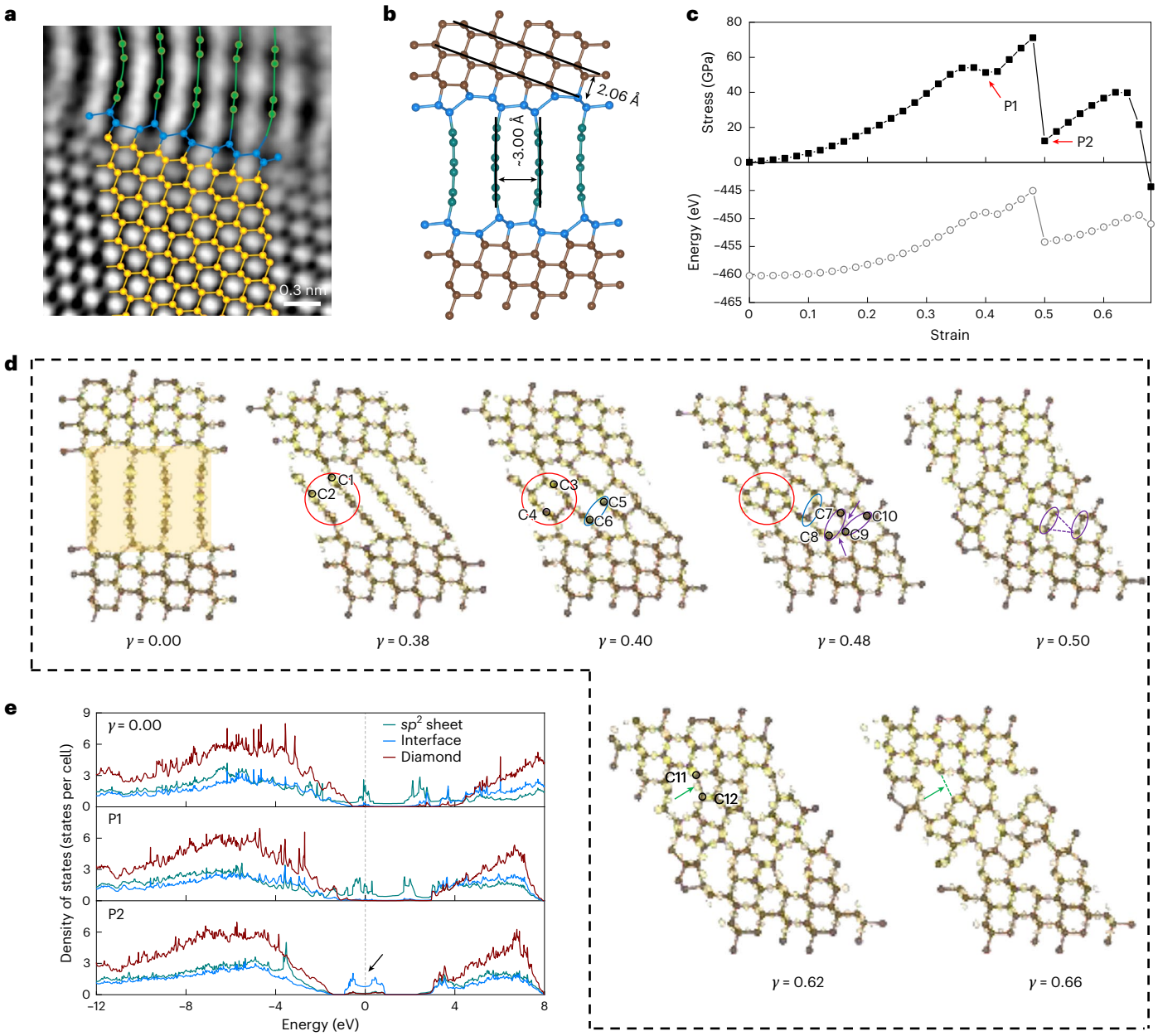

Fig. 5 | DFT simulation results for a simplified model of the MWCNT/diamond interface. a, ABF-STEM image of the coherent MWCNT/diamond interface overlaid with its ball-and-stick structural model. **b**, Structural model. The interface, sp^2-hybridized sheet and diamond-structured atoms are coloured in blue, green and brown, respectively. **c**, Stress–strain relation calculated with the structural model and the corresponding energy–strain relation under shear strain parallel to the interface. **d**, Structural snapshots of the structural model corresponding to electron localization function maps at different key strains. **e**, Density of states for the structural model at equilibrium conditions and the phase-transitioned polymorphs. The Fermi level was set to zero.

the dispersed and weakened crack propagation energy was consumed by the mixed cracking modes.

Crack deflection was quantified at two scales (Extended Data Fig. 7). At the submicrometre scale (Extended Data Fig. 7d), the lengths of undeflected segments in Vickers indentation cracks averaged ~0.6–1.0 μm, matching the diamond grain sizes (~0.8–1.3 μm), which indicates transgranular fracturing with deflections at grain boundaries or CNT-rich regions. At the nanoscale (Extended Data Fig. 7k), undeflected segments in tensile-test cracks averaged ~5–8 nm, which correlates with the CNT spacing and nanotwin thickness (~4–8 nm). This was driven by MWCNT pull-out and bridging and defect structures (stacking faults and nanotwins). We used these multiscale analyses to statistically quantify the crack tortuosity and confirm the effective crack deflection by the 3D MWCNT network across length scales. The synergistic strengthening mechanism of the composite can be summarized as follows. The partially transformed MWCNT network provides continuous pathways for large-scale crack bridging and energy dissipation via pull-out and bridging. Moreover, the fully transformed diamond segments and the ubiquitous ultrathin covalent interfaces together establish robust, direct chemical anchors that ensure the immediate and efficient load transfer from the hard diamond matrix to the tough nanotube network. This integrated 3D network and 3D interface work in concert to achieve simultaneous load sharing and distributed energy dissipation.

To elucidate the toughening mechanism at the atomic scale, we constructed a simplified model based on its heterogeneous structural

bonding features (Fig. 5a). The critical connection between our planar DFT model and the tubular MWCNTs stems from the stress-induced flattening of MWCNT walls observed under HTHP conditions. Our STEM image (Fig. 2e) verifies that a segment of an MWCNT fibre in the high-stress region formed a robust interface with the adjacent diamond grains. High-resolution TEM characterizations (for example, Fig. 2g and Extended Data Fig. 3) reveal that the bonding configuration at the MWCNT/diamond interfaces formed under HTHP is locally analogous to the graphite-to-diamond transition interface. Specifically, the curved MWCNT walls were compressed into flattened segments—with localized curvature approaching zero at their central regions[7]—driven by the intense compressive stress between MWCNTs and the bonded adjacent diamond grains, as illustrated in Fig. 2e. In these flattened regions, the atomic arrangement of MWCNTs becomes structurally equivalent to planar carbon segments with closed sp^2-bonded lateral terminals (a key distinction from graphite segments featuring open sp^2-bonded lateral terminals). Therefore, our planar sp^2 sheet/diamond interface model effectively captures the actual physicochemical environment of the transformation zone.

The model comprises several layers of the diamond structure units and sp^2-hybridized sheets, which are reasonably reduced from sp^2-bonded MWCNT structures. The model allows us to investigate its plastic response under a shear strain parallel to the interface (Fig. 5b). Both the calculated stress–strain and energy–strain relations (Fig. 5c) exhibit a sawtooth pattern, indicating several response stages and involving several bond breaks and changes in the chemical bonding configuration[42–44].

Structural snapshots and the corresponding electron localization function maps at key strains (equilibrium, several peaks and valleys, and failure strains) reveal the following sequence of events. At a strain of 0.38 (the first peak in Fig. 5c), the sp^2-hybridized sheets and the diamond portion were significantly deflected. Subsequently at a strain of 0.40, the C1 and C2 atoms on two columns of sp^2-hybridized sheets (highlighted in the red circular regions) formed bonds, resulting in the formation of a carbon polymorph P1. The stability of P1 was verified using ab initio molecular dynamics simulations (Extended Data Fig. 8). When the strain was increased to 0.48, the stress gradually rose to the second peak. The C3 and C4 atoms along with the C5 and C6 atoms (marked in blue ellipses) located on two other columns of sp^2-hybridized sheets also bonded, forming a denser sp^3-hybridized lattice. At a strain of 0.50, the C7–C9 bond in the near-interfacial region broke, causing a sharp drop in the stress. This event led to the reconfiguration of the surrounding atoms (highlighted in purple) and the formation of a carbon polymorph P2, characterized by C7–C8 and C9–C10 bonding. Notably, P2 was stable and continued to produce the next stage of plastic response until the fracture of the C11–C12 bond (marked with green arrows) at a strain of 0.66, leading to the final failure (Extended Data Fig. 8).

A density of states analysis indicates that, unlike the Gradia structure with sp^2–sp^3 mixed interface atoms[7], the macroscopic conductivity exhibited by the composites primarily originates from the sp^2-hybridized components and the contribution of a small number of interface atoms (Extended Data Fig. 9). Up to a strain of 0.40, the metallic character of the formed P1 polymorphs remained localized within the sp^2-hybridized sheets. However, as the phase transition progressed further, the metallic character of the resulting P2 phase can be attributed to the initial interface atoms (indicated by the black arrow in Fig. 5e), where the sp^2-hybridized sheets are fully bonded to each other so that some interface atoms adopt a sp^2-hybridized configuration. Importantly, the diamond atoms remained strongly covalently bonded throughout the entire deformation process.

These results demonstrate that the localized sp^2–sp^3 transformations within the sp^2-hybridized sheets lead to the formation of stable carbon polymorphs, which enable the subsequent plastic response stage where the phase transition between carbon polymorphs continues to occur under large strains. This continuous phase transition effectively dissipates the strain energy and prevents a brittle fracture, thereby enhancing fracture toughness.

Conclusions

In summary, we have successfully developed an extrinsic toughening strategy that allows us to synthesize a 3D-MWCNT–diamond composite with a heterogeneous structure containing a 3D continuous network under HTHP conditions. This composite has an exceptional combination of high fracture toughness (36.4 MPa $m^{1/2}$ as tested by SENB) and high hardness (91.6 ± 3.1 GPa as tested at 29.4 N). This notable performance is attributed to the robust interfacial bonding between MWCNTs and diamond, which is facilitated by mixed sp^2–sp^3 bonding and by the strategic incorporation of fibrous MWCNTs that bridge the gaps between diamond units to maintain the continuity of the atomic interface. The uneven stress distribution of diamond powder during high-pressure compression plays a pivotal role in achieving toughening through high-pressure interface engineering, which allows MWCNTs to bond with the diamond while preserving their fibrous structure. Our findings, corroborated by advanced characterization techniques and DFT simulations, offer profound insights into the toughening mechanism, which encompasses crack deflection, stress dispersion and energy dissipation. This groundbreaking structural architecture strategy represents a milestone in the development of superhard materials and composite ceramics, promising cost reductions, lifetime extensions and future technical innovations across various practical applications.

Methods

Synthesis of bulk 3D-MWCNT–diamond

We used commercially available high-purity diamond powder (grain size 0.8–1.3 μm and 99.99% purity; Zhongnan Jiete Super Abrasives) and MWCNTs (inner diameter 5–10 nm, outer diameter 10–20 nm, length 10–20 μm and >95% purity; Xianfeng Nanomaterials Technology) as the starting materials (Extended Data Fig. 1a,b). The as-received MWCNTs were dispersed in a dispersant solution containing aromatic groups with the aid of ultrasonic agitation. The diamond powder was added to this solution and ultrasonically agitated to give 95 wt% diamond plus 5 wt% MWCNTs in the solution. The initial volume fraction of MWCNTs was ~8.3 vol%, calculated using the density of diamond (3.52 g cm^{-3}) and the skeletal density of the MWCNTs (~2.1 g cm^{-3}). The mixed slurry was ball-milled (8000M, SPEX) for 5 h to ensure thorough de-agglomeration and the uniform dispersion of MWCNTs among the diamond particles. To prevent density-driven sedimentation during drying, the slurry was placed on a heated magnetic stirrer (HS-12, JOANLAB) and continuously stirred until completely dry, yielding a homogeneous mixed powder. This powder was subsequently heat-treated at 450 °C in a resistance furnace (KSL-1700X, Hefei Kejing) to ensure complete volatilization of the residual dispersant. This step confirmed that removal of the dispersant did not affect the final density or microstructure of the composites.

The powder blends (Extended Data Fig. 1c) were packaged with Ta foil and pre-compressed into discs (3.5 mm in diameter and 2 mm in thickness) with a relative density of ~70%. HTHP experiments were performed with a 20-MN double-stage large-volume multi-anvil system with a standard assembly 14/8 (ratio of octahedron edge length and truncated edge length). The temperature was measured with type D W–Re thermocouples, and the pressure was estimated from previously obtained calibration curves. The synthesized samples were ~3 mm in diameter and ~2 mm thick.

Preparation of the tested 3D-MWCNT–diamond samples

The synthesized samples were treated with acid to remove any packaging and then polished at ambient pressure using a diamond paste. We used polished samples to measure the Vickers hardness, as STEM

specimens and as micrometre-sized beams for the SENB tests. STEM specimens and the micrometre-sized beams were prepared using a focused ion beam (FIB; Helios G4 PFIB). In the initial stage of the milling process, a 1 nA current and 30 kV were used to dig two craters separated by a thin wall. The wall was then extracted as a thin foil for STEM observation or further processed into a test beam, with both ends connected to the bulk sample (Supplementary Fig. 5). A tungsten tip was used to extract the foil for STEM, and a lower current, ranging from 0.1 nA to 10 pA, was used to polish the sample to the desired dimensions.

Sample characterization

The diamond–MWCNT powder blend was observed by SEM with a FIB to investigate the dispersion of the MWCNTs and mixing. The hardness of the samples was characterized by a Vickers hardness tester (FV-700B, Future Tech) with an applied load of 29.4 N for 15 s. The Vickers hardness was determined with equation (1):

$$H_v = 1854.4\frac{F}{L^2} \quad (1)$$

where F (newtons) is the applied load and L (micrometres) is the average diagonal of the Vickers indentation. The indentation fracture toughness was calculated with equation (2):

$$K_{IC} = 0.0166\left(\frac{E}{H_V}\right)^{0.5} \times \frac{F}{C^{1.5}} \quad (2)$$

where E = 1,050 GPa is the Young's modulus of diamond[45] and C is the average length of cracks measured from the indent centre.

STEM measurements were performed by an aberration-corrected scanning transmission electron microscope equipped with double Cs correctors (CEOS) for the condenser lens and objective lens (ARM-200F, JEOL). ABF images were acquired at acceptance angles of 11.5–23.0 mrad. SENB tests were conducted in a scanning electron microscope equipped with an in situ mechanical test instrument (Hysitron PI-85). We prepared micrometre-sized test beams (about 10 µm in length, 0.4 µm in width and 1.3 µm in height), each with a precut notch in the centre point of the underside, to minimize the size effect, as shown in Supplementary Fig. 5. The SENB tests and fracture toughness calculations are described in more detail elsewhere[5], and information about the dynamic testing processes can be found in Supplementary Video 1. A tensile fracture test was conducted on an FEI Tecnai F30 TEM system using an electrical holder from PicoFemto. A foil of the MWCNT–diamond composite was welded onto a copper FIB holder with a diameter of 3 mm. A tungsten tip was used to contact the left side of the foil. A piezo manipulator moving at a rate of about 0.01 nm s^{-1} then applied a tensile force (Supplementary Video 2).

DFT simulations

The DFT simulations were performed using the Vienna ab initio simulation package (VASP)[46] with the projector augmented wave method[47] and with the local density approximation in the form of Ceperley–Alder[48,49] as the exchange-correlation functional. We adopted an energy cutoff of 520 eV, an energy convergence criterion of 10^{-6} eV per cell and a force convergence criterion of 10^{-3} eV Å. We used Monkhorst–Pack k-mesh gamma-centred grids of 9 × 13 × 1 (ref. 50). The stress–strain response was determined via the ADAIS code[51]. The schematic diagrams showing atomic models and electronic structures involved in this work were all created with the VESTA[52] and SPaMD[53] packages.

Data availability

All data supporting the findings of this study are available in the main text and Supplementary Information.

References

1. Yan, C. S. et al. Ultrahard diamond single crystals from chemical vapor deposition. *Phys. Status Solidi A* **201**, R25–R27 (2004).
2. Nie, A., Zhao, Z., Xu, B. & Tian, Y. Microstructure engineering in diamond-based materials. *Nat. Mater.* **24**, 1172–1185 (2025).
3. Novikov, N. V., Dub, S. N. & Malnev, V. I. Fracture toughness of diamond single crystals. *J. Hard Mater.* **2**, 3–11 (1991).
4. Dubrovinskaia, N., Dub, S. & Dubrovinsky, L. Superior wear resistance of aggregated diamond nanorods. *Nano Lett.* **6**, 824–826 (2006).
5. Yue, Y. et al. Hierarchically structured diamond composite with exceptional toughness. *Nature* **582**, 370–374 (2020).
6. Huang, Q. et al. Nanotwinned diamond with unprecedented hardness and stability. *Nature* **510**, 250–253 (2014).
7. Luo, K. et al. Coherent interfaces govern direct transformation from graphite to diamond. *Nature* **607**, 486–491 (2022).
8. Németh, P. et al. Diamond–graphene composite nanostructures. *Nano Lett.* **20**, 3611–3619 (2020).
9. Zeng, Z. et al. Synthesis of quenchable amorphous diamond. *Nat. Commun.* **8**, 322 (2017).
10. Lu, L., Chen, X., Huang, X. & Lu, K. Revealing the maximum strength in nanotwinned copper. *Science* **323**, 607–610 (2009).
11. Yue, Y., Zhang, Q., Yang, Z., Gong, Q. & Guo, L. Study of the mechanical behavior of radially grown fivefold twinned nanowires on the atomic scale. *Small* **12**, 3503–3509 (2016).
12. Lu, K. Stabilizing nanostructures in metals using grain and twin boundary architectures. *Nat. Rev. Mater.* **1**, 16019 (2016).
13. Yin, Z., Hannard, F. & Barthelat, F. Impact-resistant nacre-like transparent materials. *Science* **364**, 1260–1263 (2019).
14. Chen, K. et al. Graphene oxide bulk material reinforced by heterophase platelets with multiscale interface crosslinking. *Nat. Mater.* **21**, 1121–1129 (2022).
15. Carré, H. & Daudeville, L. Load-bearing capacity of tempered structural glass. *J. Eng. Mech.* **125**, 914–921 (1999).
16. Li, F. et al. Dual-phase super-strong and elastic ceramic. *ACS Nano* **13**, 4191–4198 (2019).
17. Popov, V. N. Carbon nanotubes: properties and application. *Mater. Sci. Eng.: R: Rep.* **43**, 61–102 (2004).
18. Jian, Q., Jiang, Z., Han, Y., Zhu, Y. & Li, Z. Fabrication and evaluation of mechanical properties of polycrystalline diamond reinforced with carbon-nanotubes by HPHT sintering. *Ceram. Int.* **46**, 21527–21532 (2020).
19. Yu, M. F., Yakobson, B. I. & Ruoff, R. S. Controlled sliding and pullout of nested shells in individual multiwalled carbon nanotubes. *J. Phys. Chem. B* **104**, 8764–8767 (2000).
20. Andrews, R. & Weisenberger, M. C. Carbon nanotube polymer composites. *Curr. Opin. Solid State Mater. Sci.* **8**, 31–37 (2004).
21. Green, M. J., Behabtu, N., Pasquali, M. & Adams, W. W. Nanotubes as polymers. *Polymer* **50**, 4979–4997 (2009).
22. Curtin, W. A. & Sheldon, B. W. CNT-reinforced ceramics and metals. *Mater. Today* **7**, 44–49 (2004).
23. Goh, P. S., Ismail, A. F. & Ng, B. C. Directional alignment of carbon nanotubes in polymer matrices: contemporary approaches and future advances. *Compos. Part A* **56**, 103–126 (2014).
24. Yang, X. et al. Centimeter-sized diamond composites with high electrical conductivity and hardness. *Proc. Natl Acad. Sci. USA* **121**, e2316580121 (2024).
25. Li, Z. et al. Ultrastrong conductive in situ composite composed of nanodiamond incoherently embedded in disordered multilayer graphene. *Nat. Mater.* **22**, 42–49 (2023).
26. Munch, E. et al. Tough, bio-inspired hybrid materials. *Science* **322**, 1516–1520 (2008).
27. Park, R. & Paulay, T. *Reinforced Concrete Structures* (Wiley, 1975).
28. Zhang, J. et al. Transparent diamond ceramics from diamond powder. *J. Eur. Ceram. Soc.* **43**, 853–861 (2022).
29. Guan, S. et al. Fragmentation and stress diversification in diamond powder under high pressure. *J. Appl. Phys.* **124**, 215902 (2018).

30. Pan, Y. et al. Extreme mechanical anisotropy in diamond with preferentially oriented nanotwin bundles. *Proc. Natl Acad. Sci. USA* **118**, e2108340118 (2021).
31. Shin, Y. A. et al. Nanotwin-governed toughening mechanism in hierarchically structured biological materials. *Nat. Commun.* **7**, 10772 (2016).
32. Ashby, M. F. *Materials Selection in Mechanical Design* 5th edn (Elsevier, 2017).
33. Tian, Y. et al. Ultrahard nanotwinned cubic boron nitride. *Nature* **493**, 385–388 (2013).
34. Tatarko, P. et al. Toughening effect of multi-walled boron nitride nanotubes and their influence on the sintering behaviour of 3Y-TZP zirconia ceramics. *J. Eur. Ceram. Soc.* **34**, 1829–1843 (2014).
35. Xu, F. M., Zhang, Z. J., Shi, X. L., Tan, Y. & Yang, J. M. Effects of adding yttrium nitrate on the mechanical properties of hot-pressed AlN ceramics. *J. Alloys Compd.* **509**, 8688–8691 (2011).
36. Liu, C. et al. Texture, microstructures, and mechanical properties of AlN-based ceramics with Si_3N_4–Y_2O_3 additives. *J. Am. Ceram. Soc.* **100**, 3380–3384 (2017).
37. Ritchie, R. O. The conflicts between strength and toughness. *Nat. Mater.* **10**, 817–822 (2011).
38. Gale, W. F. & Totemeier, T. C. *Smithells Metals Reference Book* 8th edn (Elsevier Butterworth-Heinemann, 2004).
39. Wang, H. et al. Nanostructured diamond-TiC composites with high fracture toughness. *J. Appl. Phys.* **113**, 043505 (2013).
40. Zhao, Y. et al. Enhancement of fracture toughness in nanostructured diamond–SiC composites. *Appl. Phys. Lett.* **84**, 1356–1358 (2004).
41. Zhao, B. et al. Enhanced strength of nano-polycrystalline diamond by introducing boron carbide interlayers at the grain boundaries. *Nanoscale Adv.* **2**, 691–698 (2020).
42. Li, B., Sun, H. & Chen, C. Large indentation strain-stiffening in nanotwinned cubic boron nitride. *Nat. Commun.* **5**, 4965 (2014).
43. Zhang, M. et al. Superhard BC_3 in cubic diamond structure. *Phys. Rev. Lett.* **114**, 015502 (2015).
44. Xu, T., Zheng, Z., Legut, D. & Zhang, R. Dinitrogen bonding induced metal-semiconductor transition leading to ultrastiffening in boron subnitride. *Phys. Rev. B* **108**, L180103 (2023).
45. Weidner, D. J., Wang, Y. & Vaughan, M. T. Strength of diamond. *Science* **266**, 419–422 (1994).
46. Kresse, G. & Furthmüller, J. Efficient iterative schemes for ab initio total-energy calculations using a plane-wave basis set. *Phys. Rev. B* **54**, 11169–11186 (1996).
47. Kresse, G. & Joubert, D. From ultrasoft pseudopotentials to the projector augmented-wave method. *Phys. Rev. B* **59**, 1758–1775 (1999).
48. Ceperley, D. M. & Alder, B. J. Ground state of the electron gas by a stochastic method. *Phys. Rev. Lett.* **45**, 566–569 (1980).
49. Perdew, J. P. & Zunger, A. Self-interaction correction to density-functional approximations for many-body systems. *Phys. Rev. B* **23**, 5048–5079 (1981).
50. Monkhorst, H. J. & Pack, J. D. Special points for Brillouin-zone integrations. *Phys. Rev. B* **13**, 5188–5192 (1976).
51. Zhang, S. H., Fu, Z. H. & Zhang, R. F. ADAIS: automatic derivation of anisotropic ideal strength via high-throughput first-principles computations. *Comput. Phys. Commun.* **238**, 244–253 (2019).
52. Momma, K. & Izumi, F. VESTA 3 for three-dimensional visualization of crystal, volumetric and morphology data. *J. Appl. Crystallogr.* **44**, 1272–1276 (2011).
53. Liu, Z. R., Yao, B. N. & Zhang, R. F. SPaMD studio: an integrated platform for atomistic modeling, simulation, analysis, and visualization. *Comput. Mater. Sci.* **210**, 111027 (2022).

Acknowledgements

The FIB-SEM characterization was supported by the Testing and Evaluation Center for High-performance Fibers at Beihang University. This work was supported by the Synergetic Extreme Condition User Facility (https://cstr.cn/31123.02.SECUF) via stations A9, B1 and B3.

Author contributions

X.Y., J.Z., K.C., F.H., R.Z., K.Q., T.X. and X.S. conceived the project and designed the experiments. X.Y., J.Z., F.H., T.X. and X.S. carried out the design and fabrication of the 3D-MWCNTs. J.Z., K.Q., K.C., Z.W., R.Y., X.S., F.L. and G.L. characterized the samples. J.Z., K.Q. and K.C. performed the mechanical testing. K.C., K.Q. and J.Z. performed the in situ tensile tests. R.Z. and T.X. carried out the DFT simulations. J.Z. and K.C. made the videos. X.Y., K.C., J.Z., R.Z., F.H., L.W., D.H., H.G., J.L., F.L. and Y.Z. drafted the paper. All authors discussed the results and commented on the paper.

Funding

X.Y. discloses support for the research of this work from the National Key Research and Development Program of China (Grant Nos. 2023YFA1608900 and 2021YFA1400300) and the National Natural Science Foundation of China (Grant No. 12375304). K.C. discloses support for the research of this work from the National Natural Science Foundation of China (Grant No. 51772011) and the National Key Research and Development Program of China (Grant No. 2024YFA12098000). The other authors received no specific funding for this work.

Competing interests

The authors declare no competing interests.

Additional information

Extended data is available for this paper at https://doi.org/10.1038/s44160-026-01113-5.

Supplementary information The online version contains supplementary material available at https://doi.org/10.1038/s44160-026-01113-5.

Correspondence and requests for materials should be addressed to Ke Chen, Fang Hong, Ruifeng Zhang or Xiaohui Yu.

Peer review information *Nature Synthesis* thanks the anonymous reviewers for their contribution to the peer review of this work. Primary Handling Editor: Peter Seavill, in collaboration with the *Nature Synthesis* team.

[1]Beijing National Laboratory for Condensed Matter Physics, Institute of Physics, Chinese Academy of Sciences, Beijing, People's Republic of China. [2]Eastern Institute for Advanced Study, Eastern Institute of Technology, Ningbo, People's Republic of China. [3]School of Chemistry, Beihang University, Beijing, People's Republic of China. [4]School of Materials Science and Engineering, Beihang University, Beijing, People's Republic of China. [5]College of Materials and Chemistry, China Jiliang University, Hangzhou, People's Republic of China. [6]Center for High Pressure Science and Technology Advanced Research, Beijing, People's Republic of China. [7]Institute of Atomic and Molecular Physics, Sichuan University, Chengdu, People's Republic of China. [8]Institute of Major Scientific Facilities for New Materials, Southern University of Science and Technology, Shenzhen, People's Republic of China. [9]State Key Lab of Tropic Ocean Engineering Materials and Materials Evaluation, Hainan University, Haikou, People's Republic of China. [10]These authors contributed equally: Jiawei Zhang, Keliang Qiu, Tengfei Xu, Xi Shen. ✉e-mail: chenke0119@buaa.edu.cn; hongfang@iphy.ac.cn; zrf@buaa.edu.cn; yuxh@iphy.ac.cn

https://doi.org/10.1038/s44160-026-01113-5

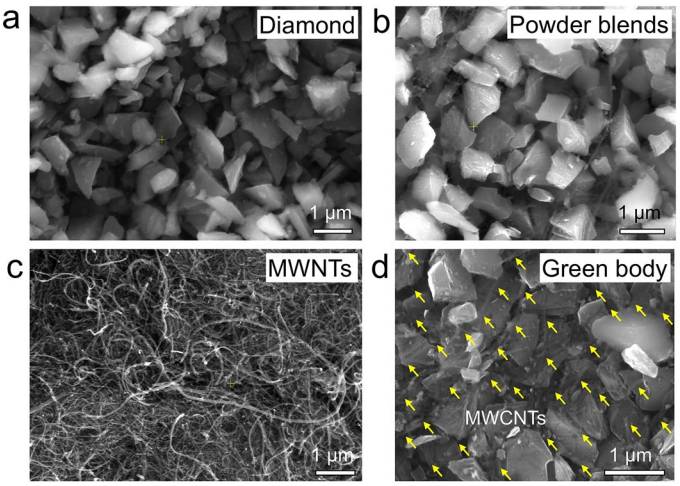

Extended Data Fig. 1 | Characterization of the starting materials. a, SEM image of the diamond powder with grain size of 0.8–1.3 μm. **b**, SEM image of MWCNTs with large aspect ratio. **c**, SEM image of diamond powders blended with MWCNTs. **d**, SEM image of the green body.

https://doi.org/10.1038/s44160-026-01113-5

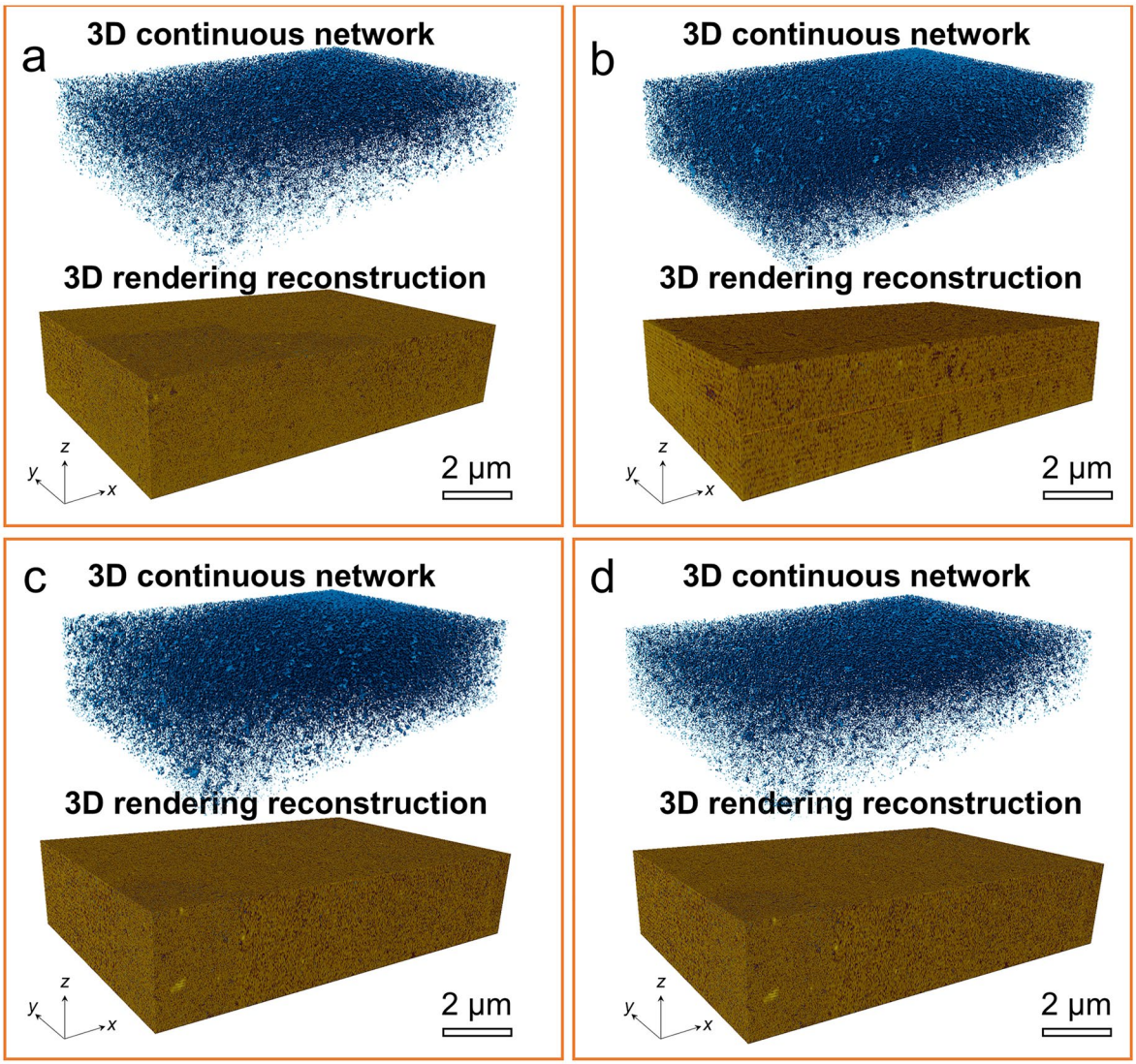

Extended Data Fig. 2 | 3D reconstruction results of sp^2-hybridised carbon networks. a, Original dataset (~3.5 vol%); **b-d**, Supplementary multi-point measurements with volume fractions of 3.53 vol% (**b**), 6.23 vol% (**c**), and 5.12 vol% (**d**), respectively. All reconstructions confirm consistent interconnected microstructures across the sample, supporting the presence of a percolating network.

https://doi.org/10.1038/s44160-026-01113-5

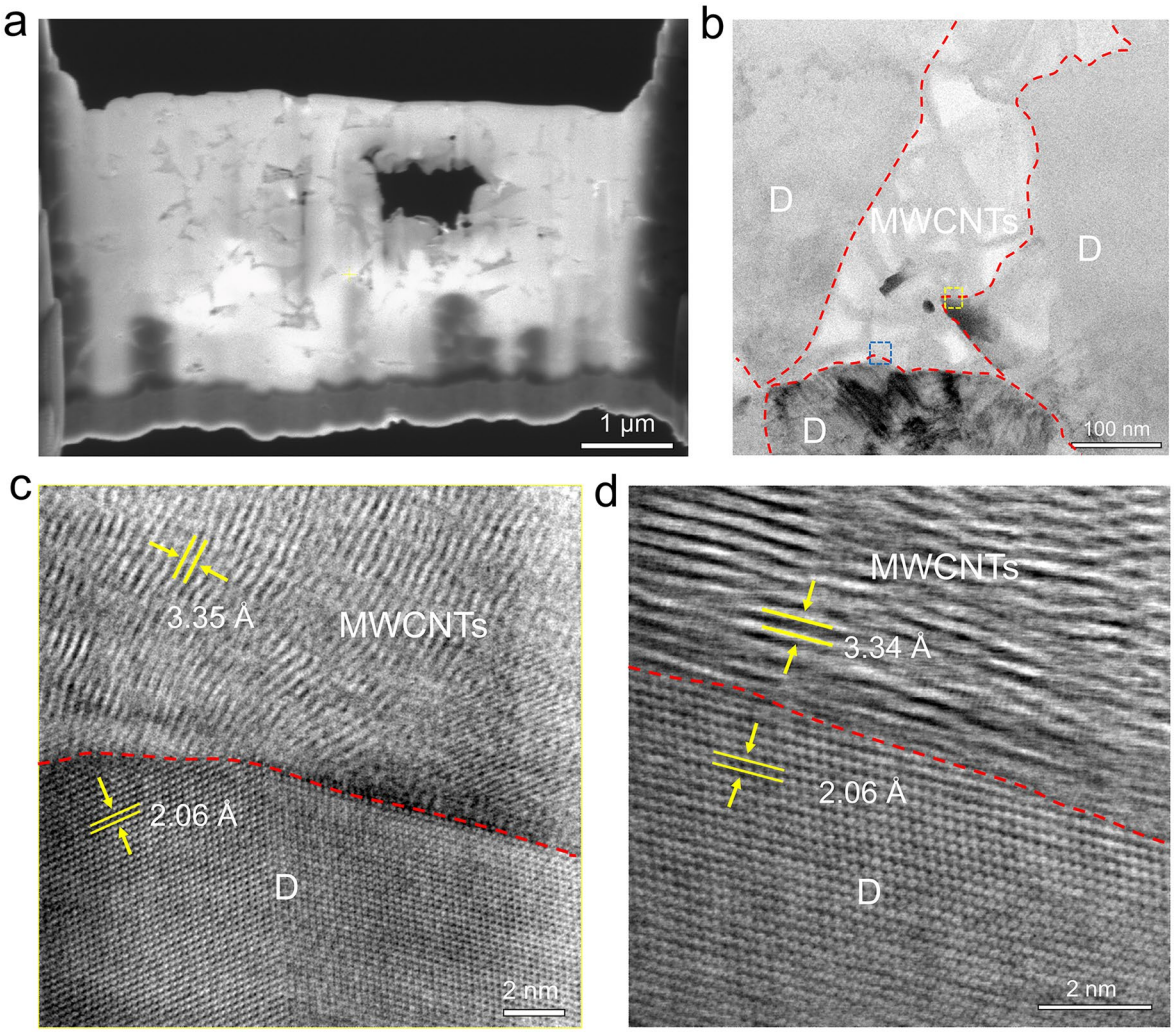

Extended Data Fig. 3 | Microstructure characterization of 3D-MWCNTs-diamond composite prepared at 15 GPa and 2000 °C, revealed by STEM. **a**, A low-magnified STEM image of a thin foil taken out to prepare STEM sample. The foil is translucent and the gap of diamond grains can be vaguely observed. **b**, A low-magnified ABF-STEM image of the thin foil, showing that MWCNTs are filled in the gaps between diamond grains, forming a 3D continuous MWCNTs network in the polycrystal diamond matrix. **c**,**d**, High-magnified ABF-STEM images of heterogenous MWCNTs/diamond interfaces, corresponding to the yellow box (c) and blue box (d) in (b), respectively.

https://doi.org/10.1038/s44160-026-01113-5

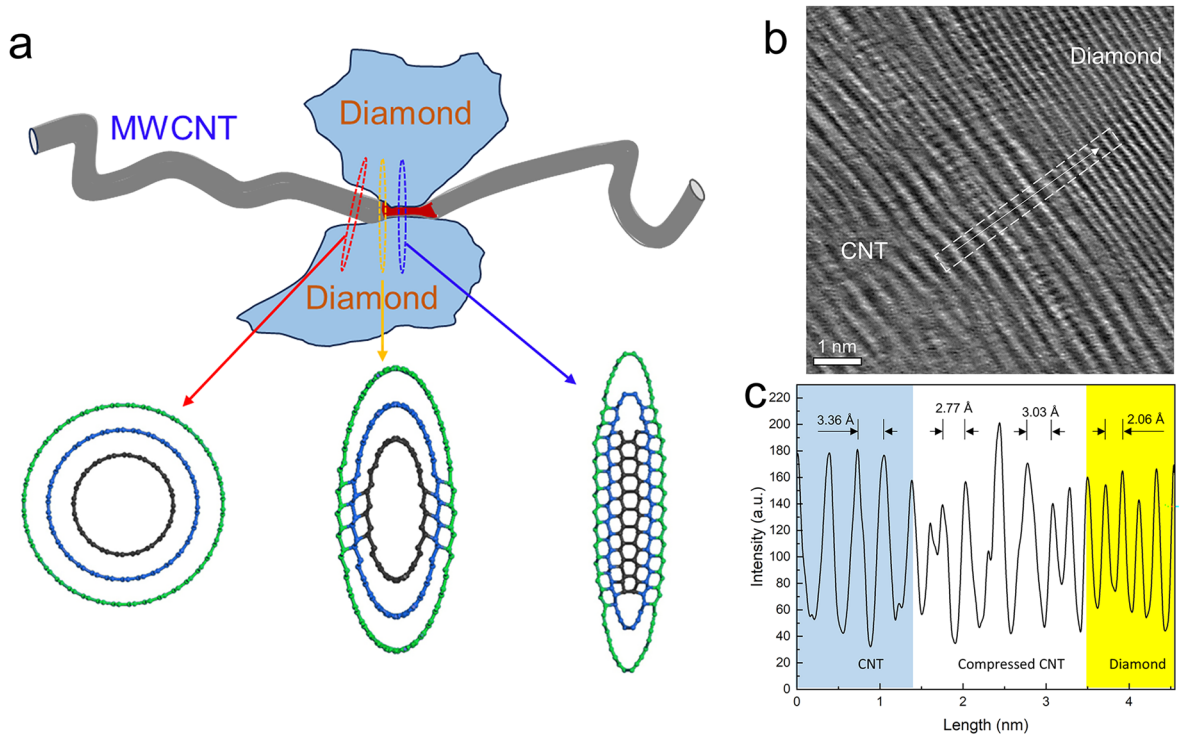

Extended Data Fig. 4 | Transformation pathway of MWCNTs to diamond. **a**, Schematic of the transformation mechanism. **b**, HRTEM image of MWCNT graphitic layers in an intermediate state of distortion and collapse. **c**, Interplanar spacing measured along the arrow in (**b**), evolving from ~3.36 Å (characteristic of curved graphitic layers) to ~2.77 Å and then to ~3.03 Å. The sequence indicates that the inner, higher-curvature CNT layers collapse and reconstruct into diamond more readily.

https://doi.org/10.1038/s44160-026-01113-5

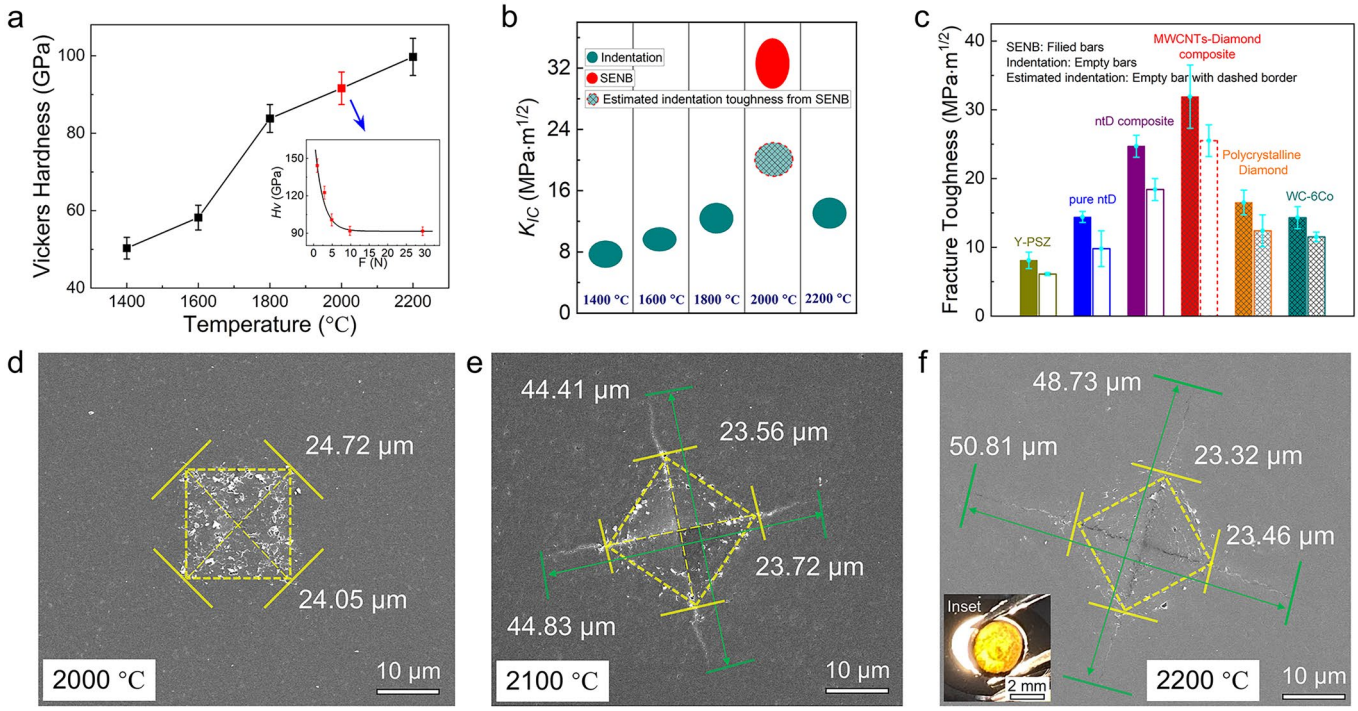

Extended Data Fig. 5 | Vickers hardness and fracture toughness of 3D-MWCNTs-diamond composites, in comparison with other materials. **a**, Vickers hardness of the composites sintered at different temperatures (1400 °C ~ 2200 °C) under 15 GPa. Inset in **a**: Vickers hardness of the composites (15 GPa, 2000 °C) as a function of the applied load. Beyond 9.8 N, Vickers hardness decreases to the asymptotic values of ~90 GPa. Data are presented as mean values +/- SD. **b**, Fracture toughness of the composites sintered at different temperatures under 15 GPa. The fracture toughness in **b** is cyan from the indentation test and red from the SENB test. **c**, Comparison of fracture toughness values from SENB and indentation measurements for commercial yttria partially stabilized zirconia (Y-PSZ, Beilong Electronics, China), pure nanotwinning diamond (pure ntD), ntD composite, polycrystalline diamond, WC-6Co, and 3D-MWCNTs-diamond composite. Data are presented as mean values +/- SD. SENB, filled bars; indentation, empty bars; Estimated indentation, empty bars with dashed border. The loads for indentation fracture toughness measurement were 49 N for Y-PSZ, and 19.6 N for pure nt-diamond and nt-diamond composite. ntD, nt-diamond. **d-f**, The typical post-indentation SEM images of indentations (29.4 N load) in composites sintered at 15 GPa and **d**, 2000 °C (crack-free), **e**, 2100 °C (short radial cracks), **f**, 2200 °C (long radial cracks). Inset in f: Optical image of the transparent sample.

https://doi.org/10.1038/s44160-026-01113-5

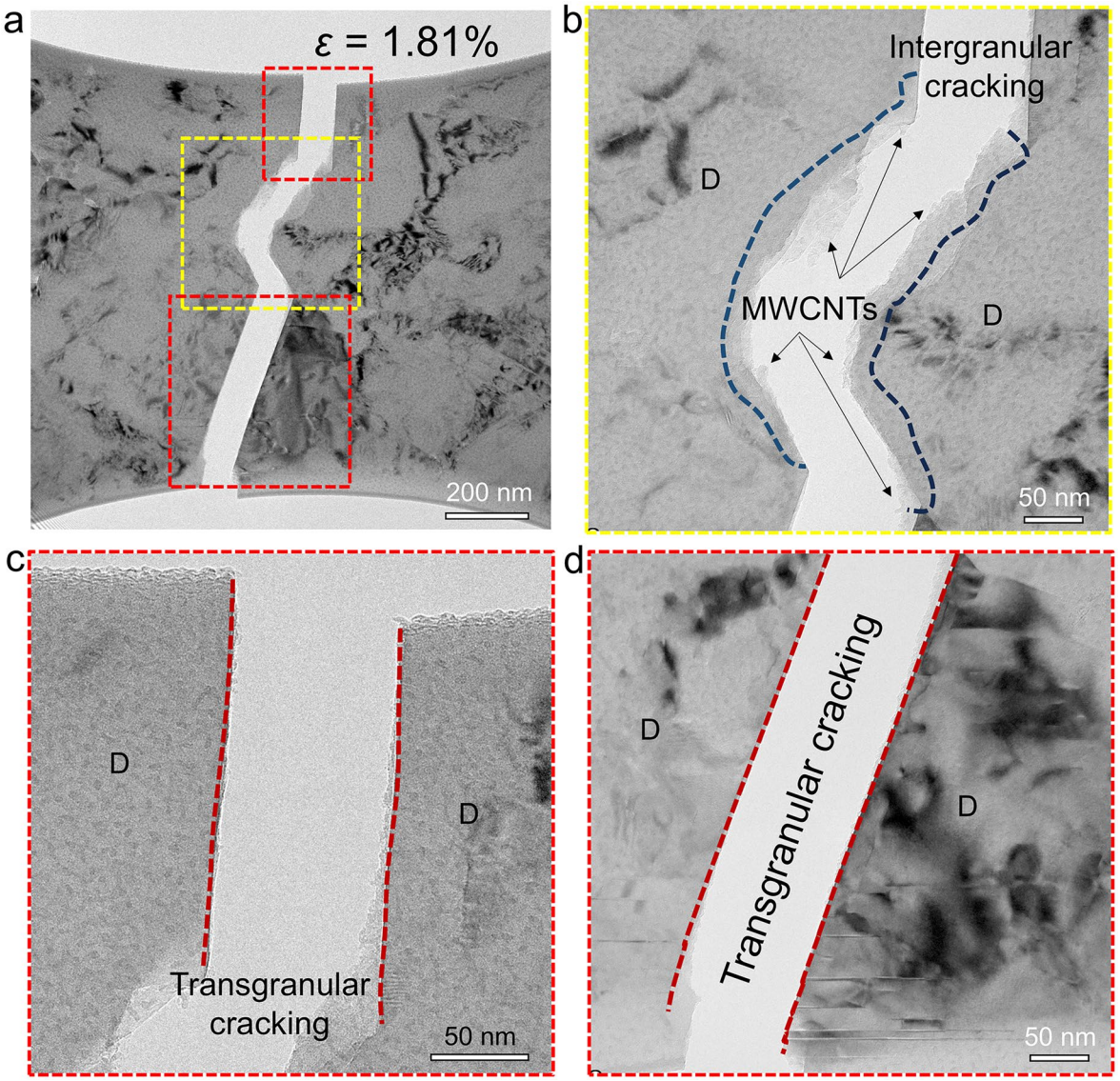

Extended Data Fig. 6 | The fracture behavior of a specially designed (bone-like) 3D-MWCNTs-diamond composite sample, by an *in situ* tensile test in the TEM. **a**, TEM image of fractured 3D-MWCNTs-diamond composite slice, corresponding to the TEM image of Fig. 4a (ε = 1.81%) in the main manuscript. **b**, Enlarged TEM image of fractured 3D-MWCNTs-diamond composite in intergranular cracking region, taken from the yellow dashed frame in **a**. **c**,**d**, Enlarged TEM images of fractured 3D-MWCNTs-diamond composite in transgranular cracking region, taken from the red dashed frames in **a**.

https://doi.org/10.1038/s44160-026-01113-5

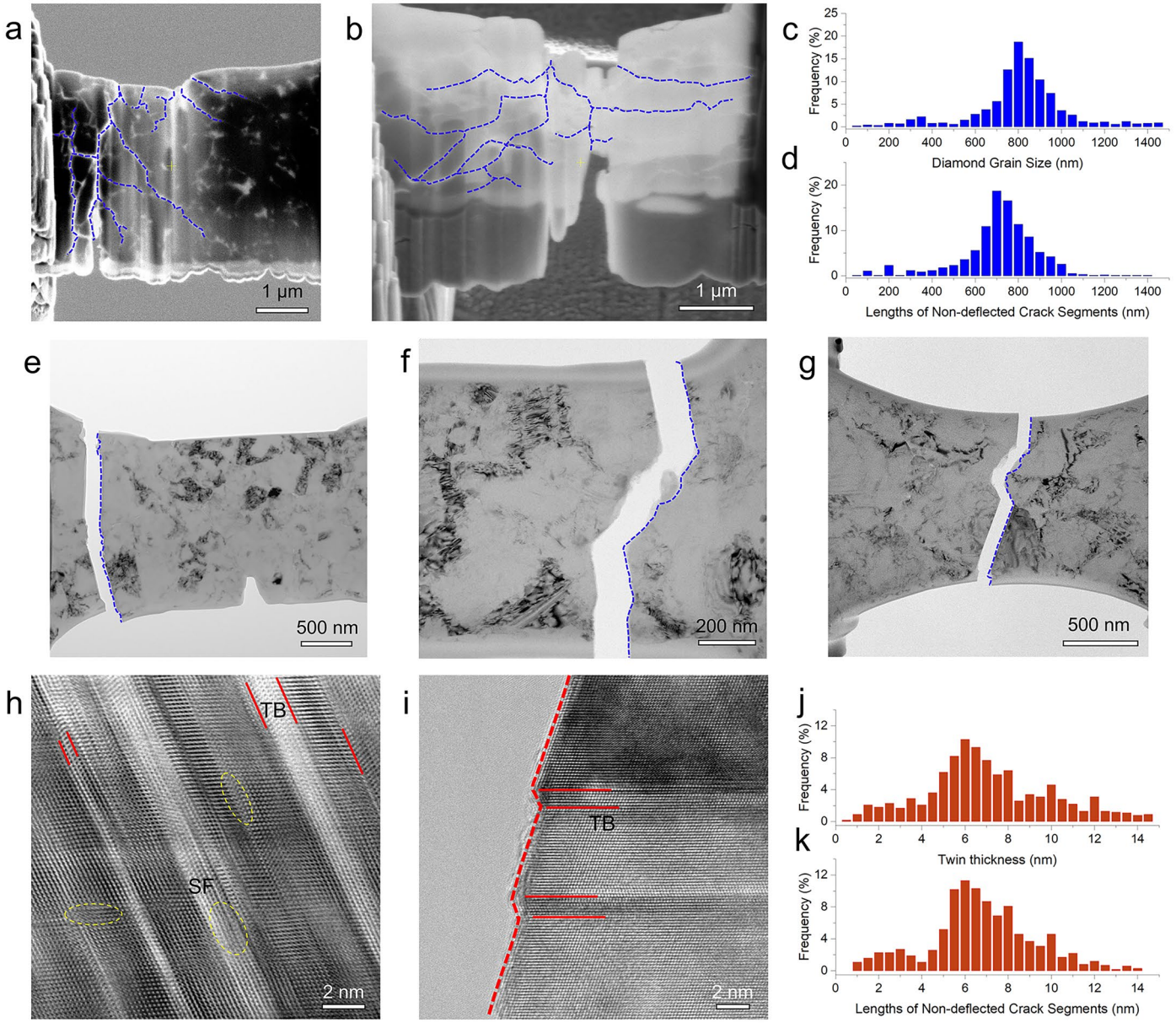

Extended Data Fig. 7 | Multi-scale quantitative analysis of crack paths in the composite. Blue and red dashed lines mark cracks used for statistical analysis of sub-micron and nanoscale crack deflection, respectively. **a-b**, SEM images of Vickers indentation cracks observed in a FIB-lift-out lamella, where stress relief during milling reveals latent crack propagation paths. **c**, Statistical distribution of diamond grain sizes. **d**, Distribution of undeflected crack segment lengths at the sub-micron scale. **e-g**, TEM images of crack paths in a tensile-tested specimen. **h**, High-resolution TEM image of diamond defect structures (stacking faults and nano-twins). **i**, High-resolution TEM image showing crack deflection at diamond defect structures. **j**, Statistical distribution of diamond twin thicknesses. **k**, Distribution of undeflected crack segment lengths at the nanoscale.

https://doi.org/10.1038/s44160-026-01113-5

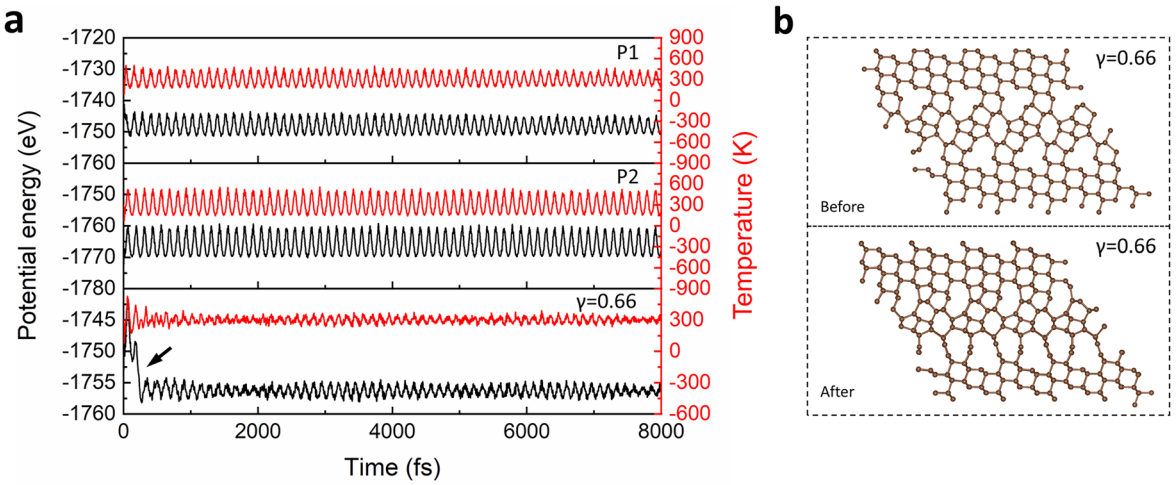

Extended Data Fig. 8 | The Ab initio molecular dynamics (AIMD) simulation results of several carbon polymorphs. a, The variation of total potential energy and temperature fluctuation for the supercells of different polymorphs during AIMD simulation of the Canonical ensemble (NVT) at 300 K. **b**, The deformed structures at the strain of 0.66 before and after the AIMD simulation. Different from the structural stability of P1 and P2 phases, for structure at strain of 0.66, there is a noticeable drop in energy (see black arrow) and a significant structural change before and after the relaxation, suggesting the instability of this phase-transitioned structure and thus the final failure of the composite during the deformation.

https://doi.org/10.1038/s44160-026-01113-5

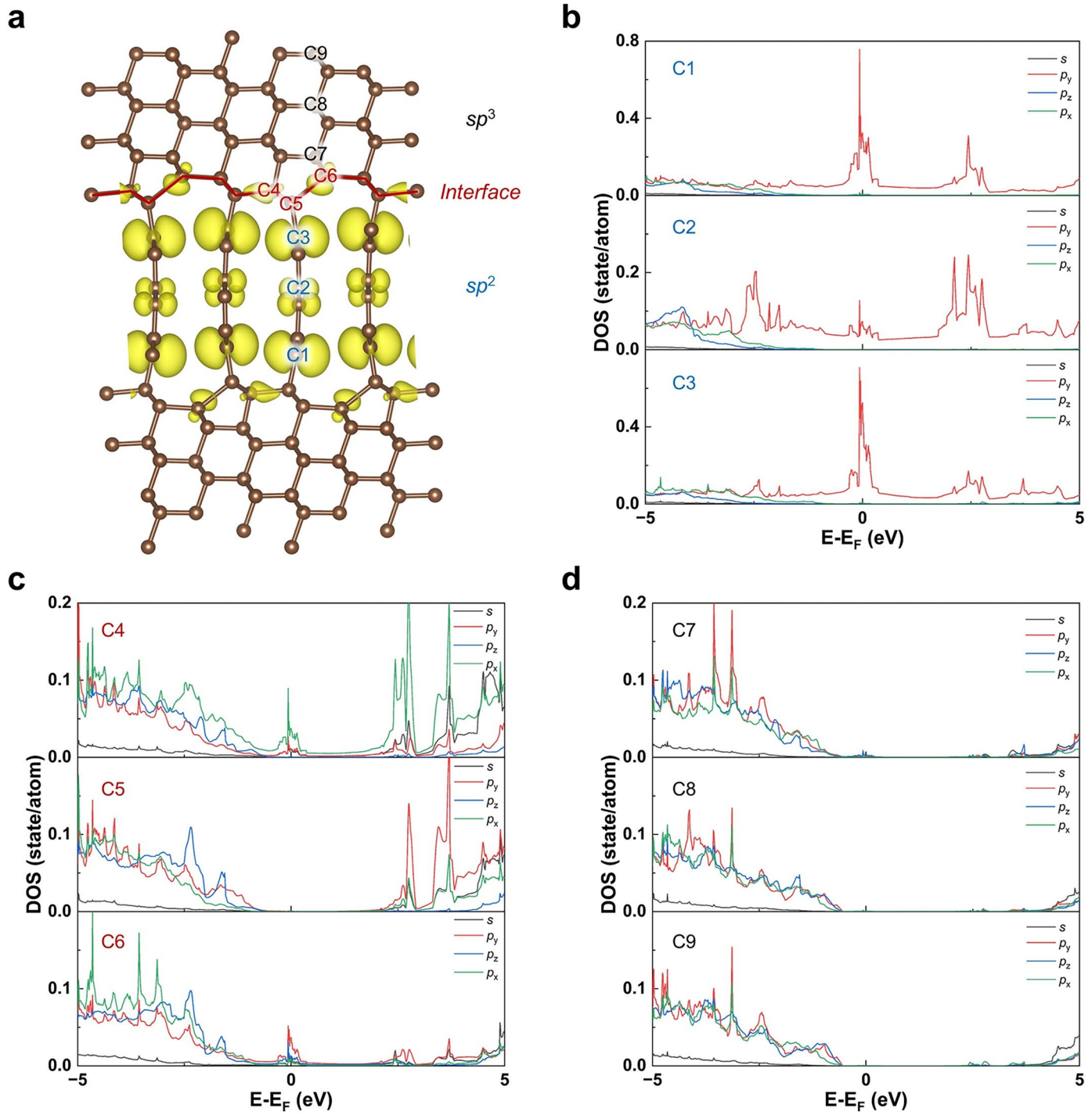

Extended Data Fig. 9 | The origin of the conductivity of MWCNTs-diamond composite. a, Calculated partial charge distributions around the Fermi level. **b-d**, Calculated orbital-resolved DOS of unequivalent atoms located in sp^2-hybridised, interface, and sp^3-hybridised regions. The atoms C1-C3, C4-C6, and atoms C7-C9 located in sp^2-hybridised, interface, and sp^3-hybridised regions are marked with blue, red and black in **a**. The interface is highlighted with red lines in **a**. The Fermi level was set to 0 in **b-d**.